

M³ spectral analysis of lunar swirls and the link between optical maturation and surface hydroxyl formation at magnetic anomalies

Georgiana Y. Kramer,¹ Sebastien Besse,² Deepak Dhingra,³ Jeffrey Nettles,³ Rachel Klima,⁴ Ian Garrick-Bethell,⁵ Roger N. Clark,⁶ Jean-Philippe Combe,¹ James W. Head III,³ Lawrence A. Taylor,⁷ Carlé M. Pieters,³ Joseph Boardman,⁸ and Thomas B. McCord¹

Received 31 August 2010; revised 28 May 2011; accepted 10 June 2011; published 9 September 2011.

[1] We examined the lunar swirls using data from the Moon Mineralogy Mapper (M³). The improved spectral and spatial resolution of M³ over previous spectral imaging data facilitates distinction of subtle spectral differences, and provides new information about the nature of these enigmatic features. We characterized spectral features of the swirls, interswirl regions (dark lanes), and surrounding terrain for each of three focus regions: Reiner Gamma, Gerasimovich, and Mare Ingenii. We used Principle Component Analysis to identify spectrally distinct surfaces at each focus region, and characterize the spectral features that distinguish them. We compared spectra from small, recent impact craters with the mature soils into which they penetrated to examine differences in maturation trends on- and off-swirl. Fresh, on-swirl crater spectra are higher albedo, exhibit a wider range in albedos and have well-preserved mafic absorption features compared with fresh off-swirl craters. Albedo and mafic absorptions are still evident in undisturbed, on-swirl surface soils, suggesting the maturation process is retarded. The spectral continuum is more concave compared with off-swirl spectra; a result of the limited spectral reddening being mostly constrained to wavelengths less than ~1500 nm. Off-swirl spectra show very little reddening or change in continuum shape across the entire M³ spectral range. Off-swirl spectra are dark, have attenuated absorption features, and the narrow range in off-swirl albedos suggests off-swirl regions mature rapidly. Spectral parameter maps depicting the relative OH surface abundance for each of our three swirl focus regions were created using the depth of the hydroxyl absorption feature at 2.82 μm . For each of the studied regions, the 2.82 μm absorption feature is significantly weaker on-swirl than off-swirl, indicating the swirls are depleted in OH relative to their surroundings. The spectral characteristics of the swirls and adjacent terrains from all three focus regions support the hypothesis that the magnetic anomalies deflect solar wind ions away from the swirls and onto off-swirl surfaces. Nanophase iron (npFe⁰) is largely responsible for the spectral characteristics we attribute to space weathering and maturation, and is created by vaporization/deposition by micrometeorite impacts and sputtering/reduction by solar wind ions. On the swirls, the decreased proton flux slows the spectral effects of space weathering (relative to nonswirl regions) by limiting the npFe⁰ production mechanism almost exclusively to micrometeoroid impact vaporization/deposition. Immediately adjacent to the swirls, maturation is accelerated by the increased flux of protons deflected from the swirls.

Citation: Kramer, G. Y., et al. (2011), M³ spectral analysis of lunar swirls and the link between optical maturation and surface hydroxyl formation at magnetic anomalies, *J. Geophys. Res.*, 116, E00G18, doi:10.1029/2010JE003729.

¹Bear Fight Institute, Winthrop, Washington, USA.

²Department of Astronomy, University of Maryland, College Park, Maryland, USA.

³Department of Geological Sciences, Brown University, Providence, Rhode Island, USA.

⁴Johns Hopkins University Applied Physics Laboratory, Laurel, Maryland, USA.

⁵Department of Earth and Planetary Sciences, University of California, Santa Cruz, California, USA.

⁶U.S. Geological Survey, Denver, Colorado, USA.

⁷Planetary Geosciences Institute, University of Tennessee, Knoxville, Tennessee, USA.

⁸Analytical Imaging and Geophysics, Boulder, Colorado, USA.

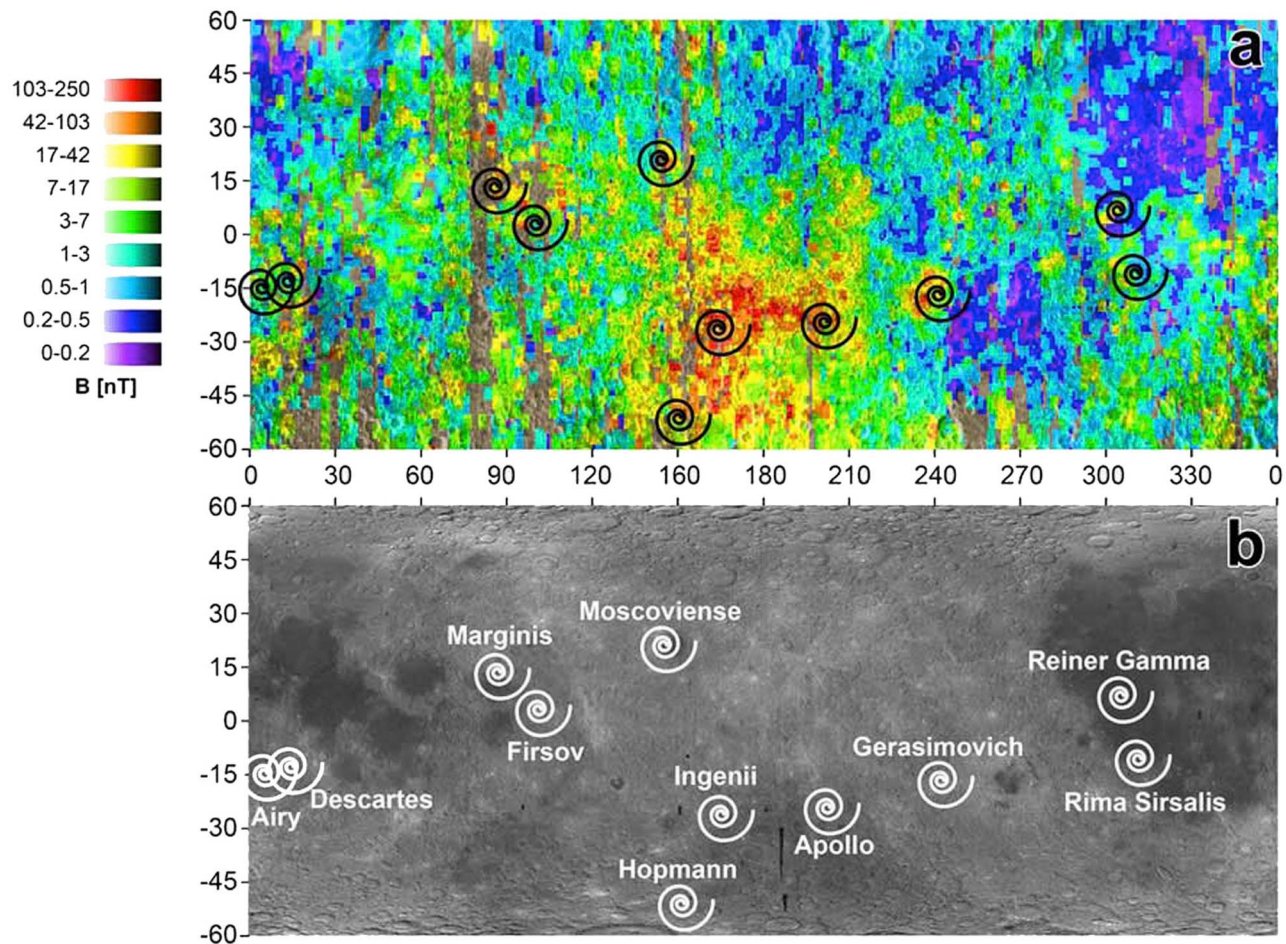


Figure 1. (a) Map of the magnetic field strength (nT) of the lunar surface measured by Lunar Prospector's Electron Reflectometer from *Halekas* [2003]. Black swirl icons depict locations of identified swirl regions. Simple cylindrical projection. (b) Location of swirls (white swirl icons), named for their location, superimposed on Clementine 750 nm reflectance map at same projection as in Figure 1a. Note that Figures 1a and 1b are centered on longitude 180° (lunar farside) and have a latitudinal range of 60°N to 60°S.

1. Introduction

[2] We examined three lunar swirls regions with imaging data from the Moon Mineralogy Mapper (M³), which rode onboard the Chandrayaan-1 spacecraft developed by the Indian Space Research Organization (ISRO). The focus swirl regions were selected as the representative of most lunar swirl types: Reiner Gamma is the most familiar lunar swirl due to its clear, identifiable markings and location on the nearside. It is located in western Oceanus Procellarum (7.5°N, 301°E). Gerasimovich is probably the best known highland swirl. It is located on the lunar farside, just west of Mare Orientale (23°S, 237°E). The swirl at Gerasimovich is associated with an isolated, high-strength magnetic anomaly. Mare Ingenii is an excellent example of a complex, multiple swirl belt. It extends over a broad region, including mare and nonmare lithologies, in the northwest of the South Pole-Aitken Basin (34°S, 163°E).

[3] Our overarching goal in this work was to characterize the major spectral differences between the swirls, interswirl regions (dark lanes), and surrounding terrain for each

studied region, and to intercompare these characteristics for similarities and differences between the three study regions. We employed statistical methods such as principle component analyses (PCA) to search for distinct spectral regions, examined apparent maturity variations on- and off-swirl, and assessed mineralogical diversity within and/or between the swirls and dark lanes. Spectral observations were then be used to constrain the models of formation for these enigmatic features.

1.1. Lunar Swirl Characteristics

1.1.1. Visible Appearance and Location

[4] Lunar swirls are high albedo and optically distinct curvilinear surface features that are found in discrete locations across the Moon's surface. A number of studies suggest that all swirls are associated with magnetic fields (Figure 1) [Hood and Williams, 1989; Richmond *et al.*, 2005; Hawke *et al.*, 2009; Blewett *et al.*, 2009]. The bright appearance and curvilinear shape of lunar swirls is often accentuated by low albedo regions that wind between the bright swirls (Figure 2).

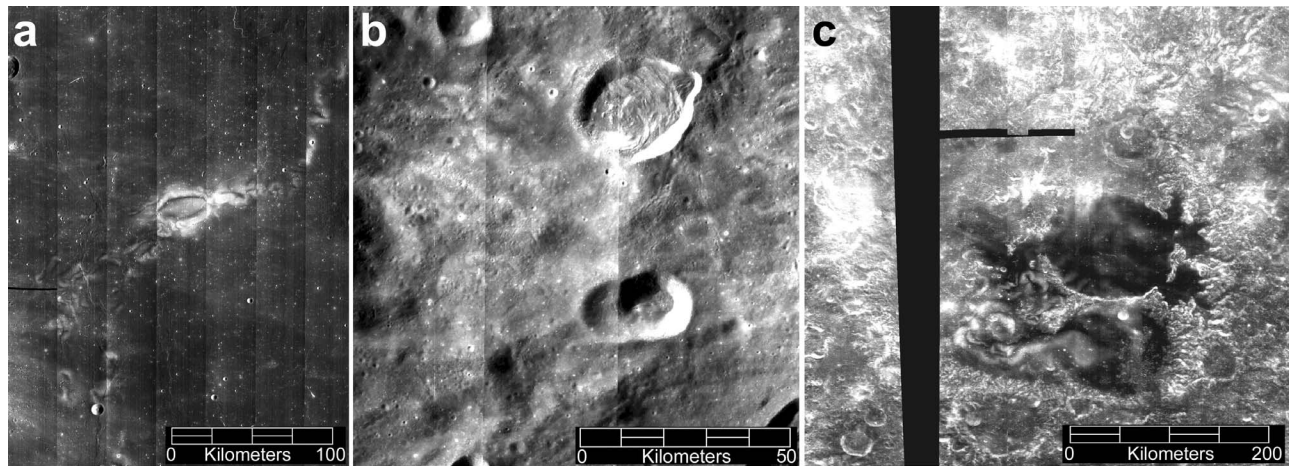


Figure 2. M³ mosaics of the three regions selected for this study shown in true color (R = 700 nm, G = 580 nm, B = 460 nm). (a) Reiner Gamma, (b) Gerasimovich, and (c) Mare Ingenii.

Swirls have been identified on both maria and highlands, and are not associated with a distinct lithology [Bell and Hawke, 1981, 1987; Pinet *et al.*, 2000; Blewett *et al.*, 2007]. The swirls have no apparent topographic association (Figure 3) (they appear to overprint the surface on which they lie), indicating that they are either a very thin layer or the manifestation of a phenomenon that is influencing surface processes. Swirls on the maria are characterized by strong albedo contrasts and sinuous morphology, whereas those on highland terrain may be less prominent and exhibit simpler shapes such as single loops or diffuse bright spots. Analysis of the strong photometric anomalies at the Reiner Gamma Formation suggest that the steepness of the phase function is not correlated with albedo and that swirls may be young features [Shevchenko *et al.*, 1994; Pinet *et al.*, 1995; Kreslavsky and Shkuratov, 2003].

1.1.2. Maturity and Spectral Characteristics

[5] Swirls appear less optically mature than their surroundings, indicating they are either fresh exposures from a recent resurfacing event or they have been spared the ravishes of space weathering. Space weathering is a process that affects the surfaces of all airless Solar System bodies, and is caused by the relentless bombardment by solar wind ions

and micrometeorites. The effects of space weathering include an overall decrease in visible to near-IR reflectance, attenuation of mafic absorption features and introduction of a strong positive slope (spectral reddening) [Pieters *et al.*, 1993]. These changes are attributed to the production of amorphous coatings on grain surfaces and tiny blebs of metallic iron, known as nanophase iron (npFe⁰) [Hapke, 2001; Noble *et al.*, 2007].

1.1.3. Magnetic Anomalies

[6] Every lunar swirl is coincident with a lunar magnetic anomaly, although not every magnetic anomaly has a visually identifiable swirl. The Moon currently does not have an active dynamo with which to generate a magnetic field, and it is debated whether one ever existed [Fuller, 1974; Fuller and Cisowski, 1987; Lawrence and Johnson, 2009; Garrick-Bethell *et al.*, 2009]. Nevertheless, orbital mapping by the Apollo 15 and 16 subsatellites and Lunar Prospector show regions of remanent magnetism in discrete locations of the lunar surface. The origin of these magnetic anomalies is still debated. Models for creation of the magnetic anomaly *independent* of swirl spectral characteristics include one that began with the observation that several of the magnetic anomalies are antipodal to the younger, large

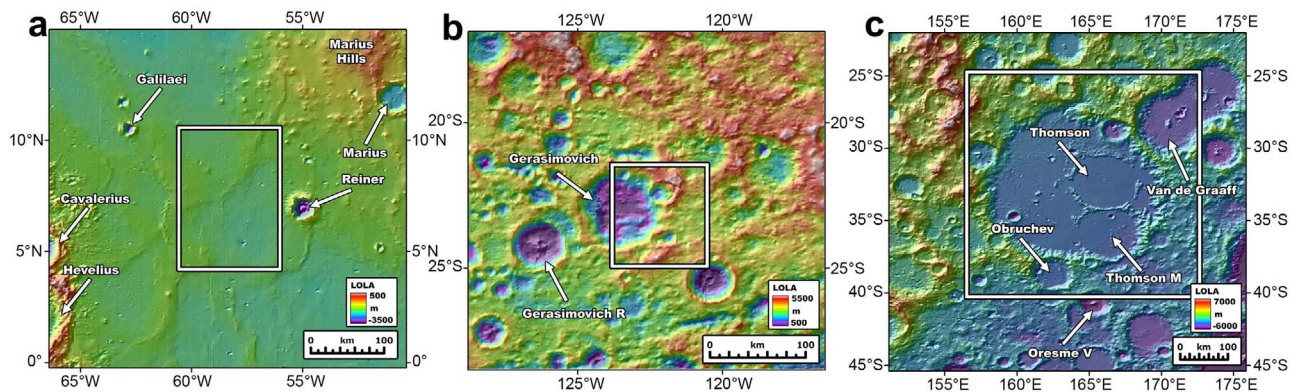


Figure 3. Lunar Reconnaissance Orbiter (LOLA) topographic information for the three swirl regions. White box delineates boundaries of studied regions shown in Figure 2.

impact basins [Hood *et al.*, 1979; Wilhelms, 1987]. Magnetization of these antipodal regions could occur in the presence of an amplified magnetic field. An amplified field could result from a plasma cloud generated by the basin forming impact interacting with a weak magnetic field present at the Moon at the time of basin formation [Hood and Vickery, 1984; Hood and Huang, 1991; Hood and Williams, 1989; Richmond *et al.*, 2005; Hood and Artemieva, 2008]. An unusually thick and/or strongly magnetized deposit of basin ejecta has been invoked to explain swirls, such as the Reiner Gamma Formation, that are not antipodal to a basin [Hood *et al.*, 2001]. The magnetized surface has also been modeled by impact-induced currents and seismic waves ringing the planet [Kletetschka *et al.*, 2009].

[7] Other models for the origin of the magnetic anomalies that are directly tied to models for the formation of the swirls are the comet impact and meteoroid swarm. These are discussed below. The origin of the magnetic anomalies is outside of the scope of this work. Although their existence and influence on spectral data must be included, we do not need to know the mechanism that created them to model the formation of the lunar swirls.

1.2. Hypotheses for Swirl Formation

1.2.1. The Meteoroid Swarm/Comet Impact Models

[8] There are two swirl formation models that suggest the swirls were produced by a relatively recent impact event involving a shower of fine fragments from the tidal disruption of a low density body prior to impact [Schultz and Srnka, 1980; Pinet *et al.*, 2000; Starukhina and Shkuratov, 2004]. These are, however, discussed together here as variations of one model. In the meteoroid swarm model the curvilinear swirl features and lack of topography is interpreted as reflecting complex patterns resulting from fine-grained interparticle collisions in the cloud of impacting debris and plowed target regolith. The final dust fragments of a swarm may form a halo with albedo and color differences from the substrate around the main part of the swirl [Starukhina and Shkuratov, 2004]. In the comet impact hypothesis, the sinuous form of the swirls is the remnant manifestation of the coma's turbulent flow of gas and dust [Schultz and Srnka, 1980], which scoured the very fine fraction of surface regolith, exposed fresh material, and redeposited the fine, scoured material in discrete deposits across the target surface [Pinet *et al.*, 2000].

[9] It is suggested that the comet impact could create a magnetic anomaly from magnetization of near-surface materials heated above the Curie temperature through hypervelocity gas collisions and microimpacts. Starukhina [2007] proposed that a high-speed meteoroid swarm would generate a magnetic field on airless bodies. Proponents of the comet and meteoroid swarm impact models consider the occurrence of several of the swirls antipodal to major basins to be coincidental or the result of incomplete mapping of swirl locations.

1.2.2. The Solar Wind Deflection Model

[10] The solar wind deflection hypothesis describes a process for maintaining the spectrally immature nature of the lunar swirls, and was developed in conjunction with the basin-antipode model of Hood and colleagues [e.g., Hood and Schubert, 1980; Hood *et al.*, 1983; Hood, 1987; Hood and Williams, 1989; Hood and Huang, 1991; Hood and

Artemieva, 2008] that describes the formation mechanism of the magnetic anomalies. Combined, they model swirl formation as a continuing process, which dates from the latter part of the basin formation era, specifically the upper Imbrian and later. It is unlikely that spectral analysis in the wavelength range of M³ data can address the basin antipode model. However, we can use spectra collected from the swirls and surrounding regions to assess the solar wind deflection model independently. Thus, our focus would be on addressing the idea that the swirls represent exposed silicate materials whose albedos have been selectively preserved over time via deflection of solar wind ion bombardment by preexisting strong crustal magnetic fields. According to this model, optical maturation of exposed silicate surfaces in the inner solar system is at least partly a function of the solar wind ion bombardment. This conclusion was supported by results from Kramer *et al.* [2011] using Clementine spectral data at Ingenii. They interpreted the spectral characteristics of the swirls and their surroundings at Ingenii as reflecting the importance of the solar wind on the spectral effects of space weathering, and the efficiency of solar wind ion deflection by the local magnetic field on influencing solar wind space weathering.

1.2.3. The Dust Transport Model

[11] Recently, Garrick-Bethell *et al.* [2011] proposed a new model to explain the association of swirls with magnetic fields, as well as several newly discovered spectral properties. Specifically, they proposed that the weak electric fields produced by the solar wind interaction with crustal magnetic anomalies [Longmire, 1963; Hood and Schubert, 1980] may attract or repel electrically charged fine dust that is believed to be lofted above the surface during terminator crossings [Criswell, 1972; Zook and McCoy, 1991]. Since the finest fraction of the lunar soil is bright, enriched in feldspathic material, and contributes significantly to the spectral properties of the lunar regolith, the horizontal accumulation or removal of fine dust can change a surface's spectral properties. This lofted dust may preferentially accumulate in swirl regions and increase the swirls' visible reflectance, as well as other spectral properties of swirls. This model can explain the brightening of swirls while permitting micrometeoroid weathering. However, it is not clear if the spectral and maturity trends observed at swirls are exactly those that are predicted by accumulation and/or removal of fine dust. The net horizontal movement of fine dust in a region would disrupt the steady state maturation process that operates elsewhere, creating dust mixtures with spectral properties unlike normal soils that have been better characterized. A challenge in testing the dust transport model with remote spectral data is that the spectral properties of the very finest dust (~1 μm diameter) have not been fully characterized.

2. Background on Selected Swirl Regions

2.1. Reiner Gamma

2.1.1. Regional Geology

[12] The Reiner Gamma swirl (Figures 2a and 3a) is located on the western equatorial nearside of the Moon and is the most intensely studied swirl. It lies in a vast mare region in Oceanus Procellarum. The dark mare provides a

contrasting background to the high-albedo swirl feature. Unlike other swirls, Reiner Gamma has a singular and prominent central feature, sometimes referred to as the “eye” or “heart”. Two “arms” or “tails” of associated daughter swirls extend linearly to the NE and SW. At certain locations, the tails expand into complex, sinuous shapes. In the present study, the central portion is referred to as the heart and the distal parts as the tail regions.

2.1.2. Previous Swirl Analyses

[13] Reiner Gamma has been observed by numerous space missions (Lunar Orbiter, Clementine, Smart-1, Kaguya, Chandrayaan-1) as well as by Earth-based telescopes. Consequently, several studies of Reiner Gamma have been performed. One of the most detailed studies was made by *Pinet et al.* [2000] using Clementine ultraviolet-visible (UV-VIS) spectral images and Earth-based observations. They concluded that the spectral characteristics of Reiner Gamma can be modeled by different size fractions of the regolith. The heart and NE tail are composed of a soil size fraction $>45 \mu\text{m}$ and the SW tail is made of the finest fraction, $<45 \mu\text{m}$. They concluded that their model results for grain size sorting supported the comet impact hypothesis [*Schultz and Srnka*, 1980; *Starukhina and Shkuratov*, 2004]. A comet impact would scour the very upper layer of the regolith, thereby removing the finest fraction of the soil ($<45 \mu\text{m}$) and creating the heart. This material would then be redistributed in the direction of the comet trajectory, laying down laterally variable and local accumulations of this finest fraction, which would create the SW tail. *Chevrel et al.* [2006] used principal component analysis (PCA) to model regolith properties, such as grain size, using Hapke parameters. Their preliminary results suggested that the variations in the parameters are consistent with the scenario proposed by *Pinet et al.* [2000].

[14] *Kreslavsky and Shkuratov* [2003] took advantage of the multi angular observations of Clementine to perform a photometric study, in particular determining the phase function steepness of Reiner Gamma. They interpreted the darker anomalies and localized bright anomalies as indicating that the surface regolith has not reached equilibrium and that the surface is indeed young. They supported the comet impact model, because they concluded it was the only mechanism so far proposed that could create an immature soil in a short amount of time. These results were updated recently by *Kaydash et al.* [2009] using multiangular images of the heart of Reiner Gamma from SMART-1’s Advanced Moon micro-Imager Experiment (AMIE) camera. The authors proposed millimeter-scale variations of the regolith texture to explain the photometric properties of the Reiner Gamma Formation. Radar observation of Reiner Gamma by *Campbell et al.* [2006] do not show evidence of different grain size for blocks larger than 10 cm (size of blocks that can be detected using a 13 cm wavelength), but these observations would not be sensitive to variations on the scale expected by *Pinet et al.* [2000] or *Kaydash et al.* [2009].

2.2. Gerasimovich

2.2.1. Regional Geology

[15] The Gerasimovich swirl (Figures 3b and 2b) is located in the farside highlands, mostly within the 86 km diameter crater Gerasimovich (22.9°S 122.6°W), and is antipodal to

Mare Crisium. The swirl is flanked by the western periphery of Mare Orientale ejecta to the east and Apollo Basin (and South Pole-Aitken Basin) to the southwest. The region has therefore witnessed several major events throughout geological time. The highland location of the Gerasimovich swirl results in lower contrast between the swirl and its surroundings as shown in Figure 2b. As a result, it is difficult to map out the exact extent of the swirl based on albedo images. Unlike other swirls which usually extend in a continuous fashion, the swirls at Gerasimovich appear to be discontinuous. This may, however, be an effect of the poor contrast between the swirls and surrounding highlands. Only one prominent sinuous loop is easily identifiable in albedo images. Other possible segments may exist, but are less easily detected. Another peculiarity of these swirls is that unlike other farside swirls which occur in association with furrowed and pitted material [*Schultz and Gault*, 1975], no such association is observed for the Gerasimovich swirls. This might be due to later modification of the area by the Orientale impact event.

2.2.2. Previous Swirl Analyses

[16] The Gerasimovich swirls have been documented in various studies [*Hood*, 1981; *Richmond et al.*, 2005; *Hughes et al.*, 2006] ever since they were first imaged by the Zond 8 spacecraft. It has been observed that these swirl locations are strongly correlated with an electron reflection maxima [*Hood*, 1981], which is an indirect indicator of magnetic field strength. Similar correlations were later obtained between high albedo swirls and the locations of strongest magnetization using Lunar Prospector low altitude magnetometer data from lunar prospector magnetometer [*Richmond et al.*, 2005]. In terms of morphology, stereopairs derived from Zond 8 data sets [*Shevchenko*, 1994] were used to infer that the swirls formed recently as they were stratigraphically overlying all other formations. Albedo estimates of the swirls and their surrounding soils were also made and compared with weakly compacted soil by Lunokhod-2 rover to assess the effect of compaction on the overall albedo. It was suggested that the trends were comparable and that high-albedo swirls possibly resulted from weak compaction of lunar regolith layer.

[17] Recent observations over the Gerasimovich swirls [*Wieser et al.*, 2010] by the Sub-keV Atom Reflecting Analyzer (SARA) instrument on Chandrayaan-1 have led to imaging of a 360 km wide minimagnetosphere, over the Gerasimovich area, inferred by the observation of deflected neutral hydrogen atoms with energies greater than 150 eV. This observation has important implications for the formation mechanisms of swirls and the long standing debate on the role of energetic particles in the space weathering process.

2.3. Mare Ingenii

2.3.1. Regional Geology

[18] Mare Ingenii (Figures 3c and 2c) is one of several isolated basalt “ponds” in the northwest corner of South Pole-Aitken (SPA) basin [*Yingst and Head*, 1997]. The inner rim is ~ 325 km in diameter [*Wilhelms*, 1987], and although the Pre-Nectarian impact [*Wilhelms*, 1987] was certainly large enough to create a multiringed basin, any outer ring is unrecognizable due to unusual, furrowed terrain which surrounds the basin. Stratigraphic relationships indicate that the furrowed terrain formed roughly contemporaneously with the

Imbrium impact event [Stuart-Alexander, 1978], and its occurrence has been attributed to the convergence of seismic waves [Schultz and Gault, 1975; Richmond et al., 2005] and/or a concentration of ejected material from Imbrium impact [Haskin, 1998; Stuart-Alexander, 1978].

[19] Mare volcanism likely originated from two large, adjacent impact craters, Thompson (~120 km in diameter) and Thompson M (~100 km in diameter), both of which lie within the basin perimeter (Figure 3c). Basalt flows exceeded the rims of these large impact craters and overflowed to the west, and were likely stopped by Ingenii basin's western rim boundary. A clear delineation of Ingenii's western mare boundary is limited by the extent and complexity of superposed ejecta largely from O'Day Crater. Impact gardening has subsequently mixed O'Day ejecta deposits with the underlying thin mare basalt and deeper basin floor, creating a surface Stuart-Alexander [1978] mapped as "Light Plains Deposits".

2.3.2. Previous Ingenii Swirl Analyses

[20] The lunar swirls at Mare Ingenii are very complex owing to their unusual geographic setting as well as the variety of sizes and shapes of the swirls themselves. Some of the swirls are easily identified on the mare, however, the task of distinguishing swirls that occur in the northwestern "light plains deposits" or from bright, highland ejecta has likely been the cause for a paucity of focused analysis of the region. In the literature, Mare Ingenii and its swirls have been included mostly as part of broader studies. Stuart-Alexander [1978] mapped Ingenii basin, mare fill, swirls, light plains, and the "furrowed terrain" surrounding the basin as part of the geologic map of the central farside of the Moon. Hood et al. [2001] and Richmond et al. [2005] included Ingenii in their works relating the several swirl regions, associated magnetic anomalies, and other geologic features to their occurrences antipodal to major post-Imbrian basin impacts. Mare Ingenii's swirls were among several photometric anomalies investigated using data from the AMIE instrument on board SMART-1 [Kaydash et al., 2009].

[21] Until now detailed spectral analysis of the swirls at Mare Ingenii has been limited to Clementine UVVIS and NIR data. Chevrel et al. [1998] first focused on the region with the purpose of determining whether spectral similarities exist between different swirl regions, and whether spectral characteristics could be associated with variations in the Moon's magnetic field (using Lunar Prospector magnetometer and electron reflectometer data). They found that the continuum positive slope became increasingly blue (flattened) moving from the regions surrounding the swirls to the swirl centers. They concluded that the observed spectral characteristics are consistent with the finest fraction of the lunar soils being locally stripped off and redistributed as from a comet impact. Garrick-Bethell et al. [2011] noted similar characteristics for several lunar swirls including Ingenii's, but modeled the high albedo swirls as a redistribution of the finest soil fraction by electrostatic levitation. Kramer et al. [2011] mapped the swirls and mare at Ingenii, and used Clementine spectral data and the population of fresh impact craters to demonstrate that the swirls' optical immaturity is not the result of a recent resurfacing event. They interpreted the spectral characteristics of the swirls and

their surroundings as reflecting the efficiency of the local magnetic field in influencing solar wind space weathering.

3. Data and processing

[22] The M³ spectrometer was a guest instrument on Chandrayaan-1, the Indian Space Research Organization's (ISRO) first mission to the Moon [Goswami and Annadurai, 2009]. Almost the entire lunar surface was imaged by M³ in 85 spectral bands and at 140 m/pixel (the spatial resolution was reduced to 280 km/pixel in the last 2 months of the mission when the spacecraft climbed to 200 km). The M³ Level-1B data for optical period (OP) 1 have also been registered by ray tracing each M³ spatial element on the lunar surface to a LOLA-derived lunar reference frame [cf. Boardman et al., 2011].

[23] Orbital observations from M³ are divided into OP that differ mainly with spacecraft altitude and beta angle (the angle between the plane of the spacecraft's orbit and the vector from the sun) [cf. Boardman et al., 2011]. For accurate spectral analysis of a region it is desirable to have all orbital strips used in a mosaic derived from one OP. This is to avoid juxtaposition of two images with different illumination geometries, which can cause particular problems in data that has not been photometrically corrected. In their analysis of the volcanic domes and cones of the Marius Hills volcanic complex, [Besse et al., 2011] present some spectral effects observed in M3 data that are a result of different viewing geometries. To also avoid complications arising from unexpected spectral effects under differing viewing geometries, we use only one OP per target. Once a wavelength-dependent photometric function is available to correct all data to the same viewing geometry, the spectral characteristics of swirls imaged during different OP will be more effectively compared.

[24] Mosaics of the swirls selected for this study were produced using M³ data only. All work presented in this paper used "K"-calibrated data, and was processed through the M³ standard calibration pipeline to radiance which includes radiometric, flat field, dark current, and geometric corrections [cf. Green et al., 2011]. The radiance is divided by the solar spectrum and the cosine of the incidence angle to obtain the apparent reflectance presented in this paper. The three swirl regions have been thermally corrected [cf. Clark et al., 2011]. Photometric [Hicks et al., 2011] corrections are under development and therefore have not been applied to the mosaics used for this work. The impact of photometric effects on our interpretations is discussed in section 6.

[25] The Reiner Gamma mosaic (Figure 2a) is produced using 9 strips of OP1B data. The spatial resolution is 140 meters per pixel (m/pix), and the phase angle varies between 61 and 43 degrees, with morning (east) solar illumination (from the right). This mosaic covers the southwest swirls, the heart of Reiner Gamma and the tail. Almost all of the Reiner Gamma swirls are mapped, including those at the extreme southwest. The extreme north part of the tail is truncated because of incomplete mapping of the area during OP1B.

[26] The Gerasimovich mosaic (Figure 2b) is produced using three strips of OP2A data. The resolution is 140 m/pix,

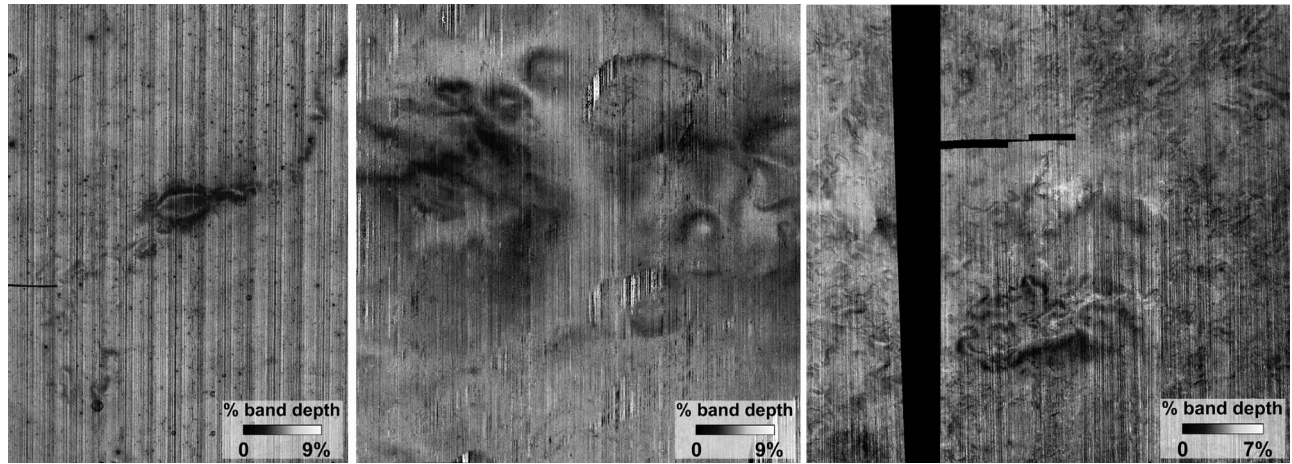


Figure 4. Parameter image of the depth of the 2.82 μm absorption feature, calculated as the percent difference in albedo from a straight-line continuum. This parameter shows the relative hydroxyl (OH) abundance of the three studied swirl regions: (a) Reiner Gamma, (b) Gerasimovich, and (c) Mare Ingenii. The swirls are recognizable by their shape and low OH abundance.

and the phase angle varies from 68 to 44 degrees. The phase angle is almost the same as OP1B, but the sun is coming from the west rather than the east as it is in OP1B. The northern part of the swirl has been imaged by M³ but is not used in that study, the southern part being brighter, which is a key element to distinguish swirls on highland.

[27] The Ingenii mosaic (Figure 2c) is produced using 7 strips of OP2C data. The data used here are from OP2C1 because this OP provided better coverage of the region [cf. Boardman *et al.*, 2011], although some of Ingenii was also imaged during OP2C3. The spatial resolution of all OP2C data is 280 m/pix because they were obtained after the altitude of the spacecraft was raised to 200 km (from the original 100 km). The phase angle varies from 46 to 25 degrees, which is a much lower phase angle than that of the Reiner Gamma and Gerasimovich mosaics, and the illumination comes from the west (afternoon).

[28] The initial spacecraft pointing was poorly known for OP2C due to the loss of both star trackers [Boardman *et al.*, 2011] This made the geometry data unreliable, and often resulted in inaccurate spatial location and orbit-to-orbit offsets in preliminary M³ data projection. As a result, we have visually corrected the orbit-to-orbit locations for our mosaic. These corrections were made by choosing tie points between adjacent strips (mainly craters) and shifting them so that morphological features match up between two adjacent strips. The shift applied to the strips was also applied to the geometric parameters to provide estimated parameters with which to appropriately derive apparent reflectance and remove the thermal contribution. The Ingenii mosaic covers the main part of Mare Ingenii's swirls and some of the swirls in western Van De Graaff Crater.

4. The Relationship Between Lunar Swirls and Surface Hydroxyl Abundance

[29] A spectral parameter can be formed from the components of a spectrum that accentuate a specific characteristic

of scientific interest. Examples of such features include the strength of absorption features, continuum slopes, reflectance ratios mineral abundances, etc. A spectral parameter image is created by applying such an algorithm to each pixel of a spectral image to derive the spatial context of the desired feature, or parameter. One such parameter used in our swirls analysis is the depth of the absorption centered on 2.82 μm (Figure 4). The absorption feature at 2.82 μm is diagnostic of the presence of hydroxyl (OH) [Keller and Pickett, 1950; Farmer, 1974; Sunshine *et al.*, 2009], and the depth of the absorption feature is a function of OH abundance. This spectral parameter image depicts the variations in depth of the 2.82 μm absorption between on- and off-swirl locations for each of the three focus swirl regions. For each of the studied regions, the 2.82 μm absorption is weaker on-swirl than off-swirl areas (Figure 5). This suggests the swirls are depleted in OH relative to their surroundings. The correlation between low OH abundance and other swirl characteristics (e.g., high albedo and low maturity) observed with M³ data is consistent with SARA observations of reduced neutral hydrogen emission from swirl regions and corresponding enhanced hydrogen emission from surrounding regions [Wieser *et al.*, 2010].

[30] The 2.82 μm absorption depth parameter, depicted in Figure 4, uses thermally corrected reflectance spectra to calculate the percent difference in albedo of the 2.82 μm (2820 nm) absorption feature from a straight-line continuum for each pixel [e.g., Clark and Roush, 1984; Clark *et al.*, 2003]:

$$\%BD_{2820} = 100 \times \left[1 - \frac{Rb}{(Cl + Cr)/2} \right] \quad (1)$$

where Rb is the maximum absorption, calculated from an average of 3 bands centered on 2.82 μm

$$Rb = \frac{Rband_{80} + Rband_{81} + Rband_{82}}{3},$$

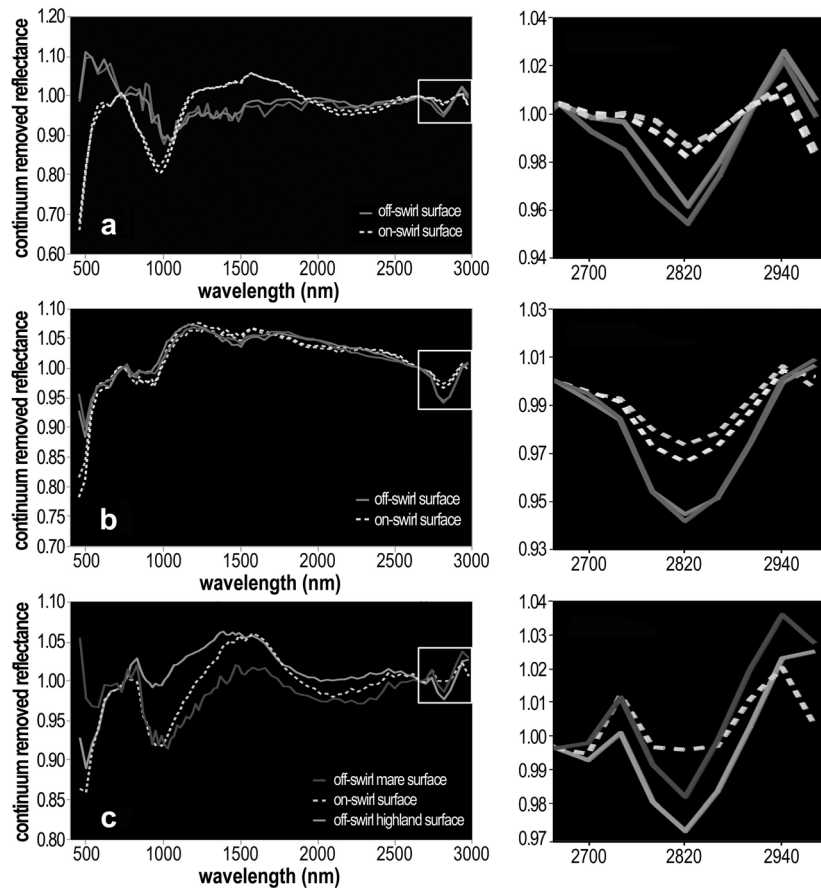


Figure 5. (left) Continuum-removed spectra collected from on-swirl (light, dashed lines) and off-swirl (dark, solid lines) surfaces at each of the study regions: (a) Reiner Gamma, (b) Gerasimovich, and (c) Mare Ingenii. This demonstrates that the OH absorption feature at 2820 nm is deeper off-swirl compared with on-swirl surfaces. Straight-line continuum calculated using the albedos at 750 nm and 2610 nm. Note that y axes are different for each region. (right) To better view the differences in the OH absorption features at each study region, close-up views of the 2600–3000 nm range from the entire spectral range in Figure 5 (left).

and the continuum from the left continuum shoulder,

$$Cl = \frac{R_{band78} + R_{band79}}{2}$$

and the right continuum shoulder,

$$Cr = R_{band84}$$

where R_{band78} is the reflectance at M³ band 78, R_{band79} is the reflectance at M³ band 79, etc. (see Table 1 for the wavelength values that correspond to the bands used in this calculation). Figure 6 is a graphical demonstration of this calculation using an off-swirl regolith spectrum from Gerasimovich (orange spectrum in Figure 13b (left)).

[31] For Gerasimovich, where the swirls are extremely difficult to delineate in albedo images, the 2.82 μm absorption depth maps provide the best view of the geographic extent of the swirls. It has been observed in M³ data that OH is often enhanced in feldspathic terrains [Pieters *et al.*, 2009]. An increased abundance of OH in the feldspathic material at Gerasimovich may help to augment the on- and off-swirl

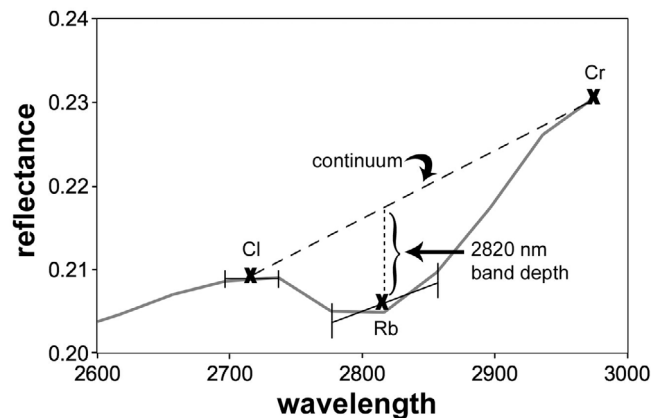


Figure 6. Graphical demonstration of the calculation of the OH parameter using an off-swirl regolith spectrum from Gerasimovich (orange spectrum in Figure 13b, left). Note the wavelength space covers a subset (2600–3000 nm) of M³'s total wavelength range (400–3000 nm) depicted in Figure 13b (left).

Table 1. M³ Band Numbers and Corresponding Wavelengths Relevant to the Calculation of the 2.82 μm Absorption Depth (Equation (1)) Used to Create Figure 4

Band	Wavelength (nm)
78	2700
79	2740
80	2780
81	2820
82	2860
83	2900
84	2940

differences in that region. In addition to simply making highland swirls easier to map, the occurrence of low OH on-swirl provides a critical constraint for evaluating hypotheses for swirl formation. It may also help to improve models for OH production on the lunar surface.

5. Analytical Techniques and Results

5.1. Principal Components Analysis

[32] Principal components analysis (PCA) is a useful tool for assessing the mathematical variability of a large number of spectra. In essence, this method views the data as a multidimensional cloud or scatterplot, and searches for the directions of variability maxima. These directions (axes or eigenvectors) are the principal components of the data and each has an eigenvalue which is a measure of the amount of variation associated with that axis. The principal components are ordered from highest to lowest eigenvalue such that the first few principal components describe the majority of the variance in the scene, while the last principal components are typically variations due to noise. Generally the number of meaningful principle components is far less than the number of dimensions, as later eigenvectors merely describe the noise in the data.

[33] In the case of imaging spectrometer data, where band to band correlation is often high, this transformation results in an image cube with new, uncorrelated axes. Because the

first principal component (PC) is typically associated with albedo variations, we mapped PC axes 2, 3, 4 into the red, green, and blue (RGB) channels of an image (Figures 7a–7c). This display results in color combinations that show much more of a scene’s spectral variability than can otherwise be shown with color combinations of channels depicting simply spectral reflectance. It is important to note that though this method effectively explores the depth of spectral variability in an image, eigenvectors are not directly equivalent to mineralogy, temperature, grain size, or other physical designations, but rather mathematical representations of the variability. Any one PC may incorporate some or no variation caused by any of these properties. We used PC axes 2, 3, 4 because they represent the maximum variability of the data. Independent of any statistical analysis of the variances, it is expected that these PC axes should represent the swirls because they correspond to the maximum spectral variations of the scene. Qualitatively it is easy to verify that a PC axis number provides legitimate spectral variation if one can observe a coherent image. If the axis number is below or too near the noise threshold, the image appears blurry or simply indistinguishable noise. Quantitative information about the PC axes and total variance for each region is shown in Figure 8.

[34] PCA is well-suited to swirl studies, as it requires no preconceived notion of what differences to expect between the swirls and interswirl dark lanes. It is effective as a mapping technique, as the first few PCAs will inherently accentuate the differences between the swirls and the surroundings. The different colors of the PCA images (Figures 7a–7c) help determine the different locations from where spectra are sampled, but the spectra can also be selected by their distribution and specificity in the PC axis numbers. In Figure 9, the Reiner Gamma swirl is easily distinguished in the scatter cloud (between the dashed lines) and clearly represents a distinct trend. Selected spectra sample this trend and show the diversity within the swirl.

[35] The PC images are shown in Figure 7a–7c and the spectra selected for analysis using these images are shown in

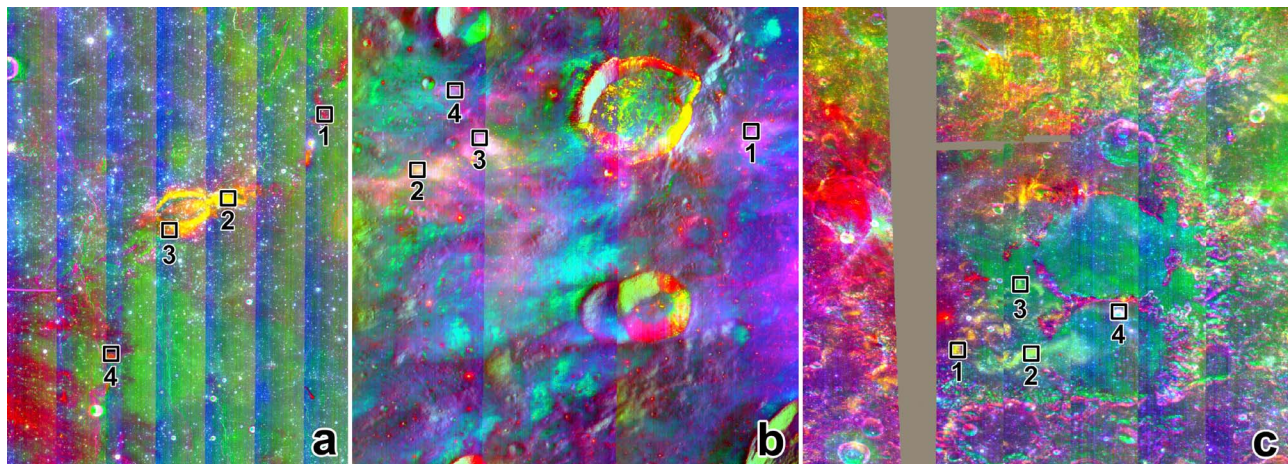


Figure 7. Color composite images using PCA axis numbers 2, 3, and 4 for the red, green, and blue channels, respectively, for (a) Reiner Gamma, (b) Gerasimovich, and (c) Mare Ingenii. Such a display results in color combinations that show much more of a scene’s spectral variability than can otherwise be shown with color combinations of regular spectral channels.

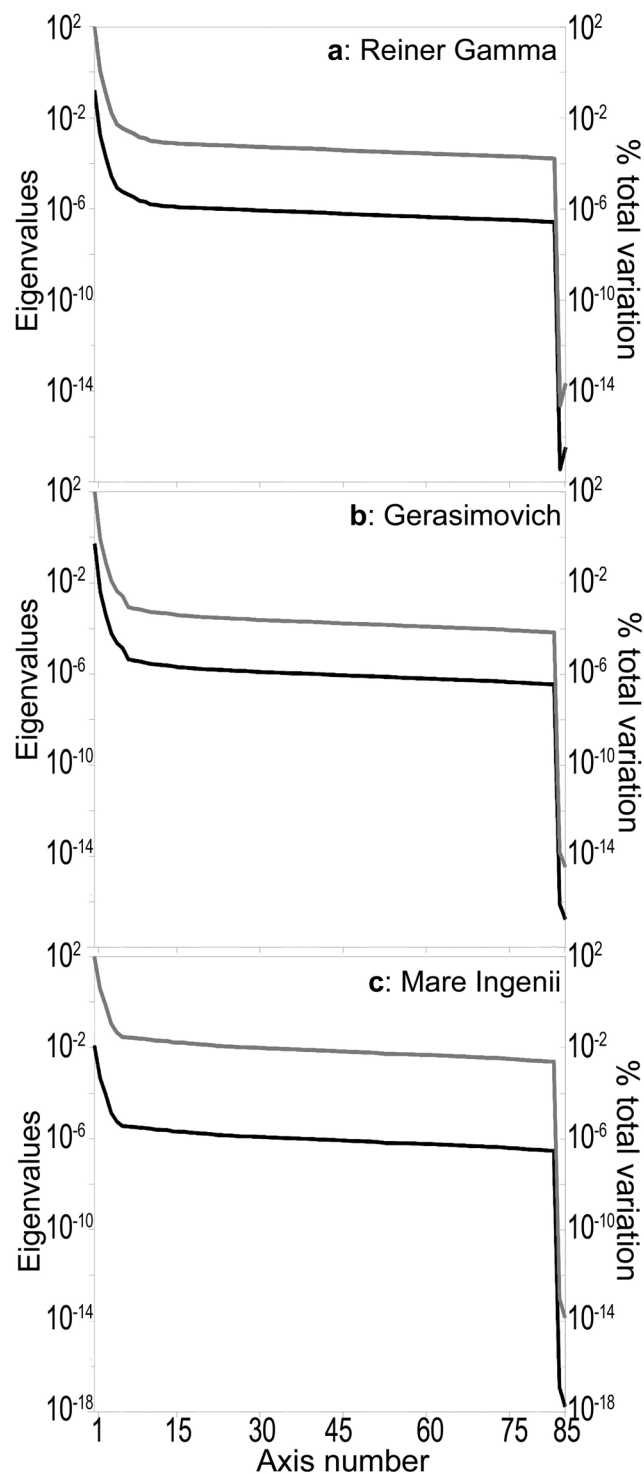


Figure 8. Eigenvalues versus axis number (black) and % total variation versus axis number (gray) for (a) Reiner Gamma, (b) Gerasimovich, and (c) Mare Ingenii.

Figure 10 (top). Continuum-removed versions of these spectra are shown in Figure 10 (bottom). Interpretation of a PCA axis is difficult and colors should not be compared between Figures 10a, 10b, and 10c because they do not express the same spectral variations. For example, yellow is

at first order correlated to albedo for Reiner Gamma and Gerasimovich; however, this is not the case for Ingenii.

[36] We do not expect the PCA axes to represent exactly the same variation in the three swirl regions because the geological setting of all the three swirls is different. Thus, there are compositional differences among the three swirl regions which results in differences in their spectral contribution in the PCA. There are also photometric differences between the three regions which have not been fully corrected in the calibration used for this study. The black boxes in Figure 7 indicate the location of the spectra presented in Figure 10. All spectra are extracted from swirls surface soils using a boxcar average of 5×5 pixels.

5.1.1. Results for Reiner Gamma

[37] For the Reiner Gamma swirl, the main swirl body shows in PC images as a very distinct yellow at its core surrounded by a more reddish color at its periphery (Figure 7a). The tails of the swirl, both to the northeast and the southwest, show in the PC image with colors similar to the periphery of the main swirl body. Spectrally, these differences manifest themselves both as a change in albedo and absorption feature strength. In Figures 10a (top) and 10a (bottom), the interior of the main swirl body has a higher albedo and deeper absorptions than both the periphery of the main body and the tails, which are quite similar spectrally. Note that while the interior of the main swirl may show a slight difference in the position of the $2 \mu\text{m}$ absorption, in general the variability across the swirl is in absorption feature depth rather than the wavelength of maximum absorption. This indicates that the mafic mineralogy is very similar across the swirls in Reiner Gamma [Pinet *et al.*, 2000]. The difference in absorption depth may be explained by variations in grain size, maturity, or composition (though if it is due to composition, it represents addition or subtraction of a component without absorption features, such as opaque minerals). The primary distinction between the yellow and red spectra (tail spectra) is a difference near $2 \mu\text{m}$.

[38] The swirl in the southwest (spectrum 4) exhibits a slightly different spectral character near $1 \mu\text{m}$ than do the other spectra. This difference is best seen in the continuum-removed spectra as a slight absorption near $1.5 \mu\text{m}$ (Figure 10a, bottom). It is possible that this difference is caused by contamination from highland material from the nearby crater Cavalerius (not visible in the images), though in that case one would expect the overall reflectance to be higher. This may indicate a difference in maturity rates on different portions of the swirl, or that several swirls, formed at different times, are superimposed on one another.

5.1.2. Results for Gerasimovich

[39] The swirls at Gerasimovich represent the highland occurrence of these features. They are difficult to detect in this geological setting owing to minimal contrast between the high albedo swirl features and bright highlands. However, PCA analysis is well suited for distinguishing features in spectral data that could otherwise go undetected. With M³ data it has been possible to isolate spectral characteristics of swirls which are different from the surrounding highlands, improving the detectability of swirls. While some of them are easily identifiable by their sinuous nature, others are more difficult to detect and need additional criteria. It is for this reason that PCA has been the best tool for analysis of the Gerasimovich swirls. Although clearly an improvement

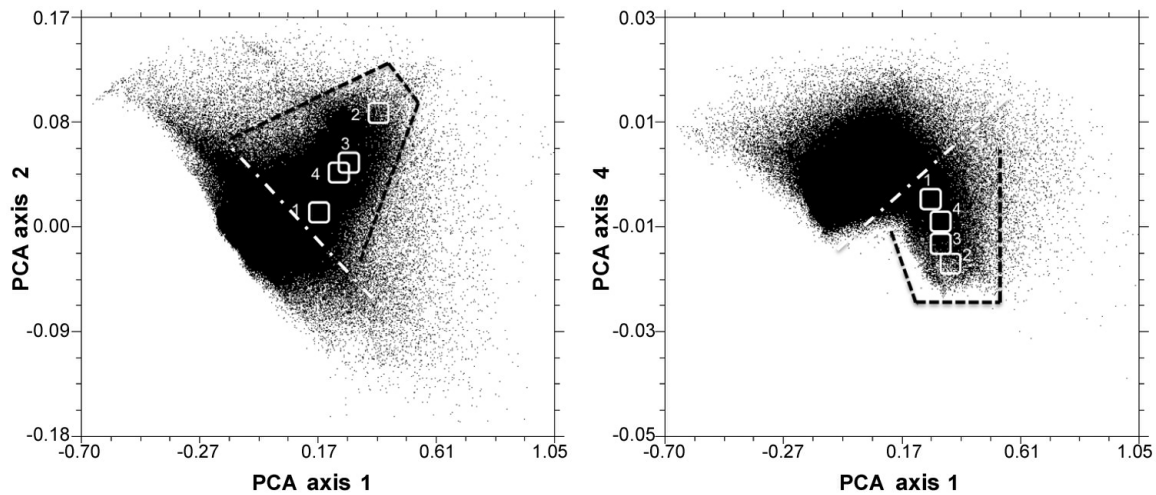


Figure 9. Scatterplots depicting the locations of the sampled spectra from the Reiner Gamma swirls (see Figure 7a) in contrasting PC axis space. (a) PC axis 1 versus PC axis 2, and (b) PC axis 1 versus PC axis 4. The dashed lines correspond to the extent of the Reiner Gamma swirls with respect to the mare background.

over a standard albedo image, the optimal PC axes for distinguishing spectral units on maria is less helpful at Gerasimovich. Therefore, we created two RGB composites using PCA data for the Gerasimovich region, one using the same PCA axes as used for Reiner Gamma and Mare Ingenii (Figure 7b), and the other using PCA axes selected specifically to highlight geologic features specific to the Gerasimovich region (Figure 11a–11c).

[40] The Gerasimovich swirls appear almost white in much of Figure 7b, though some of the swirls appear pinkish. These differences in color do not appear to be systematic, however. Similarly to the swirls at Reiner Gamma, the regions at Gerasimovich with the highest albedo exhibit the highest overall reflectance and strongest absorption features

for the region. The differences across the Gerasimovich swirls, in general, appear to be predominantly in albedo rather than absorption depth or a change in continuum. The west and middle regions (Figure 7b) appear different from the east and top, in both the PCA image and the selected spectra. Specifically, the east and top spectra do not exhibit a $2\ \mu\text{m}$ absorption feature (Figures 10b, top, and 10b, bottom). This may be due to a difference in maturity, as the $2\ \mu\text{m}$ feature is more easily diminished by normal space weathering processes than is the $1\ \mu\text{m}$ feature [Noble *et al.*, 2007]. The spectral changes that occur at Reiner Gamma and Gerasimovich are consistent with changes in optical maturity. At Reiner Gamma the spectral change is mostly the change in absorption depth and a change in continuum, which is con-

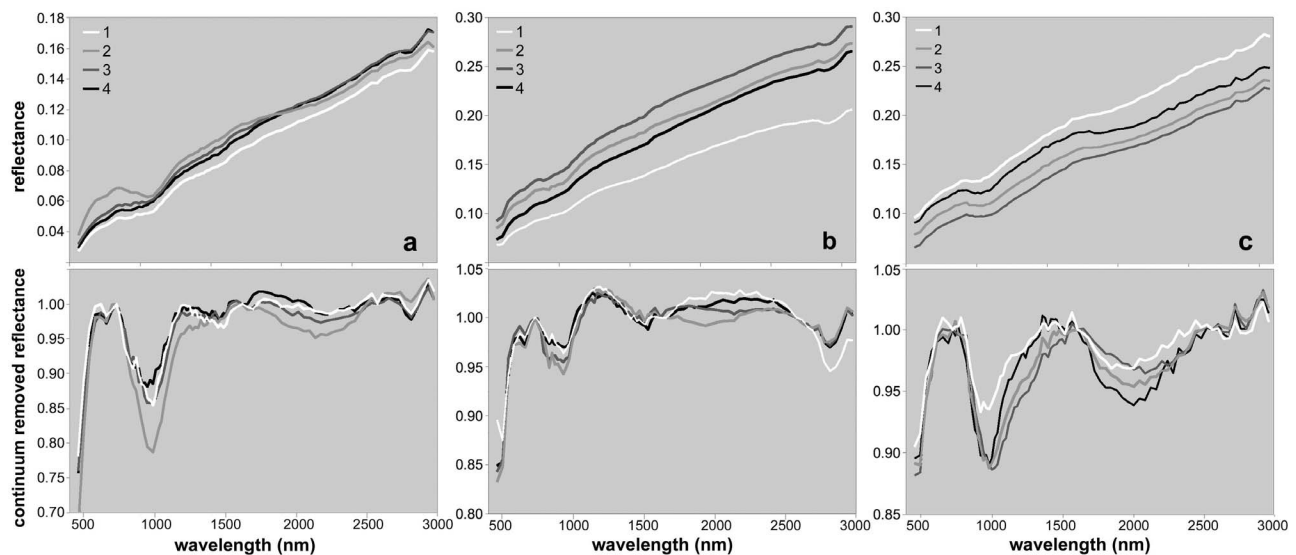


Figure 10. (top) M³ reflectance spectra of four locations in each of (a) Reiner Gamma, (b) Gerasimovich, and (c) Mare Ingenii, selected based on the respective PCA image of Figure 7. (bottom) Spectra in Figures 10a (top), 10b (top), and 10c (top) normalized to a straight-line continuum that was calculated using the albedos at 750 nm and 2610 nm.

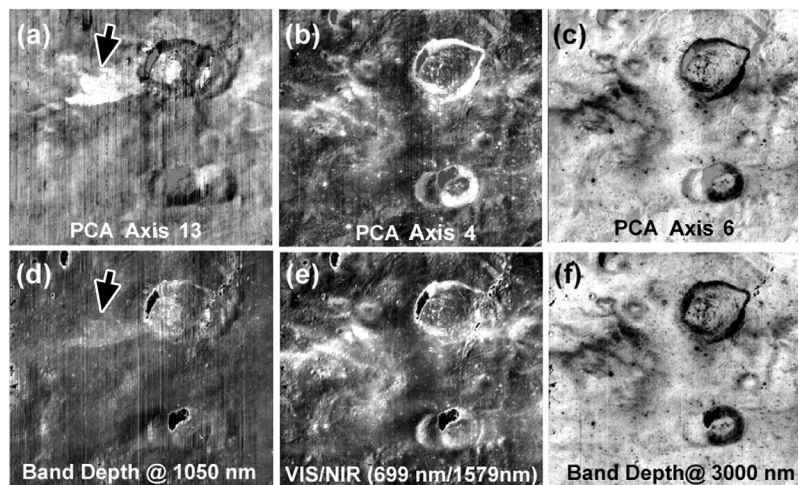


Figure 11. (a–c) PCA axes selected specifically to highlight geologic features specific to the Gerasimovich region. These PCA axis numbers are used to create the color composite image in Figure 12). (d–f) Spectral parameters that correlate with the PC axis directly above each (Figures 11a–11c) and demonstrate the scientific relevancy of these PC axes. Arrows in Figures 11a and 11d point to possible impact melt discussed in text. Deep shadows have been masked and appear black in the images.

sistent with a mare maturity trend. The spectral changes across the Gerasimovich, i.e., a change in albedo with little variation in absorption strength, is also consistent with a highlands maturity trend [Nettles *et al.*, 2011]. In addition, the position of the maximum depth of the 1 μm absorption feature occurs at a consistent position throughout the Reiner Gamma swirl region. In contrast, the maximum 1 μm absorption in spectra from the Gerasimovich swirl region occurs at a shorter wavelength, as would be expected for a slight noritic absorption in the feldspathic highlands. What is perhaps most surprising are the dramatic differences in the hydroxyl absorption feature near 2.8 μm throughout this region (see section 4).

[41] We analyzed a second set of PC axes for Gerasimovich because this region poses a particular challenge because the high-albedo swirls are not as well contrasted against the highlands as they are in mare regions. PC axis numbers 13, 4 and 6 were selected because they provide the maximum contrast between swirls and the surrounding highlands. These axes were also selected to demonstrate the scientific relevance of PCA analysis by comparing the similarities between PC axis numbers 13, 4 and 6 and three spectral parameters (compare Figures 11a–11c with 11d–11f), despite being generated in very different ways. PC axis number 13 (Figure 11a) is similar to the 1050 nm absorption depth parameter (Figure 11d). PC axis number 4 (Figure 11b) closely resembles the VIS/NIR slope using 699/1579 nm, even though the overall statistical significance of axis 13 is low (Figure 11e). PC axis number 6 (Figure 11c) resembles a measure of the depth of the absorption at 3000 nm (attributed to the presence of water, Figure 11e).

[42] The swirls are dominantly green, indicating a higher visible to near-infrared ratios (i.e., flatter continuum slope), which reflects the low optical maturity of the swirls relative to the surrounding terrain. PC axis number 13 (Figure 11a) and the 1050 nm absorption depth spectral parameter image (Figure 11d) both show a distinct, bright feature on the western portion of the crater, Gerasimovich-D (Figure 2b).

Morphologically, the feature appears to be an impact melt from Gerasimovich-D, although a distinct glass spectrum is not identified. Moving westward from the western rim of Gerasimovich-D, the melt unit appears magenta, indicating strong 1050 and 3000 nm absorption features, then transitions to orange as it converges with the green, swirl material. The stratigraphic relationship between the swirl and the melt is difficult to ascertain at present. The transition from magenta to orange indicates the continuum is becoming flatter whilst the 1050 nm absorption prevails. This kind of preservation of the mafic absorption on-swirl while the continuum changes is also seen in our analyses using small crater rim spectra (see section 5.2).

[43] Representative spectra from swirls, an impact melt unit, the mixed region (where distinguishing between swirls and probable impact melt is difficult), and the surrounding highlands were collected to evaluate the nature of these materials (Figures 12b and 12c). The spectral profiles of the swirl areas (spectra 2 and 4 of Figures 12c and 12d) have a shallower continuum slope and deeper absorption features compared to spectra from the surrounding region (blue regions of Figures 12a and 12b; spectrum 5 of Figures 12c and 12d).

5.1.3. Results for Mare Ingenii

[44] Unlike Reiner Gamma and Gerasimovich, regional differences in mineralogy complicate the swirl analysis in mare Ingenii. Spectrum 1 (Figures 7c and 10c) is the brightest of the units, but it does not have the deepest absorption features. The wavelength of maximum absorption in the 1 μm region appears to be slightly longer for spectrum 3 than the other selected spectra. The feature's shoulder at 1.2 μm is also stronger, suggesting that this unit may be slightly enriched in high-Ca pyroxene relative to the others. There are also differences in the strength of the 2 μm feature among the units, which may be due to variations in maturity or mineralogy. If the differences are due to maturity, this may support the hypothesis that the swirls formed because of magnetic shielding, with these maturity variations

implying different intensities of shielding by the magnetic field.

[45] The Ingenii swirl appears to be more complex and do not follow the trends seen for the two previous swirl regions. However, the Mare Ingenii swirl traverses a complicated terrain, and it appears that spectrum 1 is in a highlands area

while the rest are in mare. In particular, the brightest swirl material (spectrum in Figure 10c) has the weakest absorption, which is not an expected maturity trend. Consequently, the compositions of mare basalts and/or swirl itself may vary a lot.

5.2. Small Crater Rim and Ejecta Probing

[46] We analyzed M³ spectra from immature craters and regolith samples on and adjacent to swirls in our three regions of interest (Figure 13). Regolith samples are taken from no less than a 4×4 pixel neighborhood in areas that are flat and undisturbed, that is, free of slopes and immature crater ejecta as can be resolved by the data set. Immature crater spectra were obtained using the Small Crater Rim and Ejecta Probing (SCREP) procedure [Kramer, 2010] to extract compositional information from pixels on the rims and proximal ejecta of small, immature craters (1–5 km in diameter). Figure 14 shows the locations from which the spectra in Figure 13 derive. We are using these craters to see through the mature regolith, to observe the spectral character of the underlying lithology that is exposed in their ejecta [McCord and Adams, 1973; Staid and Pieters, 2000; Kramer et al., 2007, 2008; Kramer, 2010]. Analysis is focused on the rims and proximal ejecta of the craters because these are the locations that best expose the pristine bedrock while simultaneously avoiding photometric effects due to steep slopes. Impact cratering studies and analysis of impact ejecta mechanics demonstrate that near the crater rim the original stratigraphy of the impact target is inverted [Melosh, 1989]. This area represents the thickest part of the crater ejecta, and thus consists of the most concentrated, or highest proportion of native material compared to foreign material that collectively make up the regolith. Furthermore, the rim and proximal ejecta suffer the least amount of postimpact regolith build-up [Kramer, 2010].

[47] To locate immature craters from M³ data we used the VIS/NIR ratio, which uses the positive correlation between maturity and continuum slope (spectral reddening) to estimate maturity. This estimate uses the average reflectance value of three spectral bands for both the numerator and denominator.

$$\text{maturity estimate} = \frac{R_{VIS}}{R_{NIR}} = \frac{(R_{i-1} + R_i + R_{i+1})}{(R_{j-1} + R_j + R_{j+1})} \quad (2)$$

where i is the VIS albedo band and j is the NIR albedo band. For M³, $i = 9$ (~750 nm) and $j = 51$ (~1620 nm). Increasing values from this equation represent decreasing maturity.

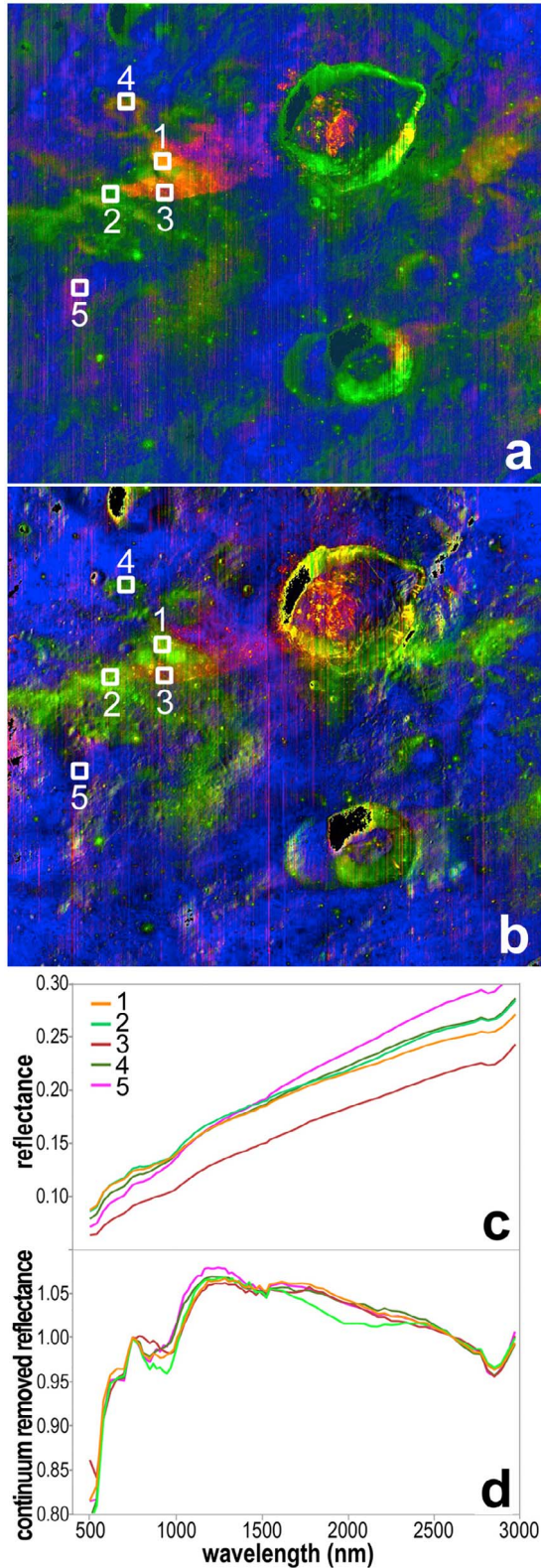


Figure 12. (a and b) RGB composites for the Gerasimovich swirl area using PCA axes $R = 13$, $G = 4$, and $B = 6$, and the corresponding spectral parameters: R is absorption depth at 1050 nm, G is Vis/NIR ratio (699 nm/1579 nm) and B is absorption depth at 3000 nm. The features used for these image composites were selected to explore the geological setting of swirls with respect to their surroundings. (c) M³ reflectance spectra of five locations in Gerasimovich selected based on PCA image of Figure 12a. (d) Spectra in Figure 12b normalized to a straight-line continuum that was calculated using the albedos at 750 nm and 2610 nm.

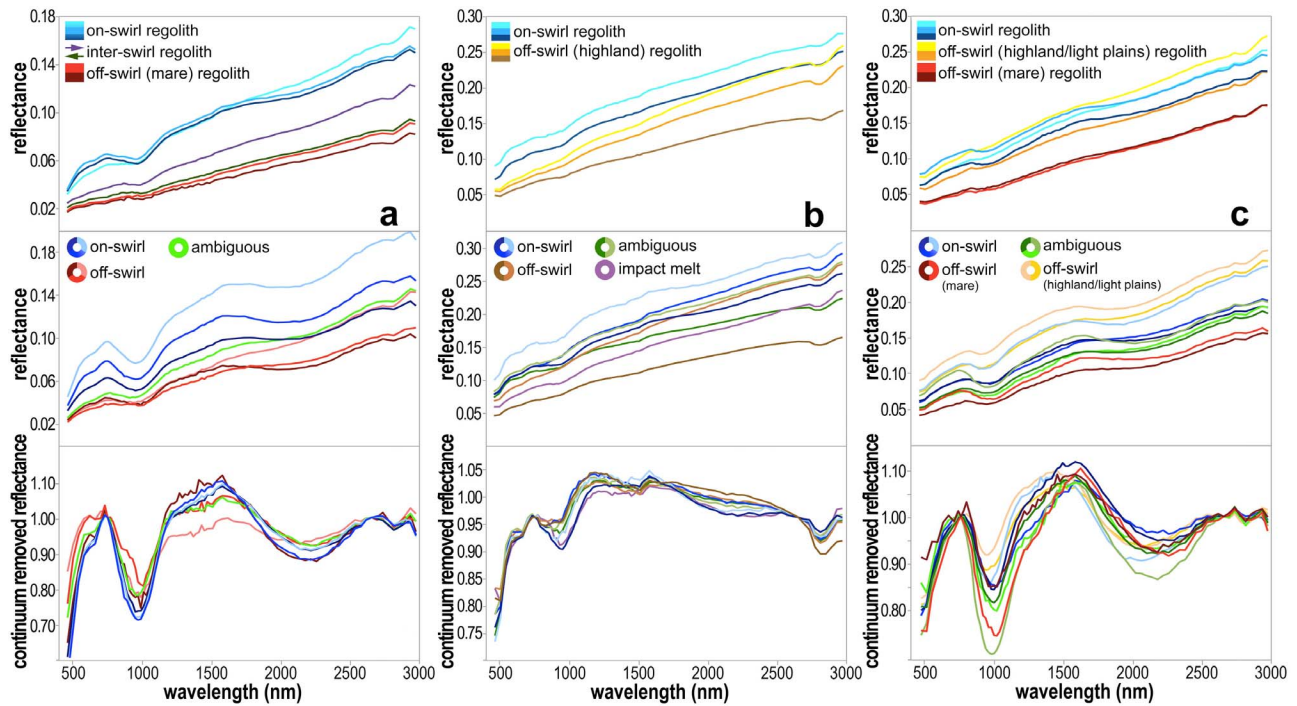


Figure 13. Spectra sampled from surface regolith and immature craters of the three swirl regions: (left) Reiner Gamma, (middle) Gerasimovich, and (right) Mare Ingenii. Colors and location from which samples derive are pictured in Figure 14. (top) Surface regolith spectra. (middle) Fresh crater spectra. (bottom) Continuum removed fresh crater spectra. Straight-line continuum calculated using the albedos at 750 nm and 2610 nm. Note that y axes are not the same for all plots.

[48] For each selected crater, SCREP defines and extracts spectral information from pixels that describe a ring, the inner circumference of which delineates the crater rim and the outer circumference such that the ring thickness is $\sim 1/10$ of the crater diameter. These data are then averaged to obtain a single spectrum for each crater that is meant to closely approximate the composition of the pristine, sub-regolith lithology exposed in that location. In this way, the

method reduces potential errors in interpretation of spectral features compared with using single-pixel spectra [Kramer, 2010].

[49] The spectral variations among immature craters that sample the same surface likely demonstrate the maturation trend in that location, however it is inappropriate to make a direct connection between a value from the maturity estimate and time because there are so many factors that go in to

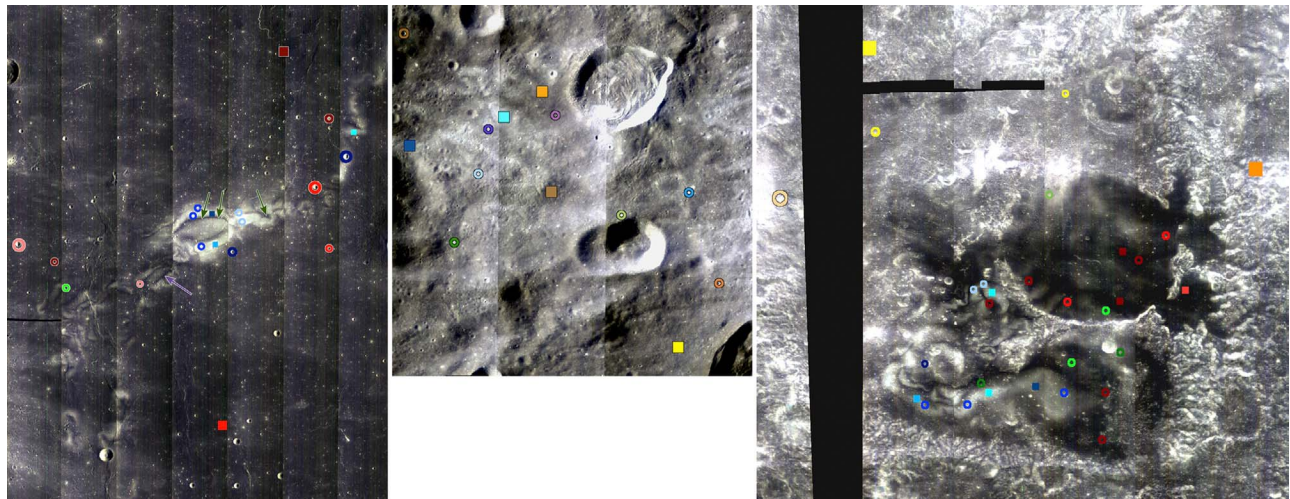


Figure 14. Locations of immature crater (rings) and surface regolith (squares and arrows) samples for spectra shown in Figure 13. Size of rings and squares does not equate to the area used to create a single average spectrum.

spectral maturation. Nevertheless, the trend for the maturing soil in a region is exemplified in spectra from fresh craters to regolith (or at least with these as end-members) because the craters used to obtain spectra representative of the bedrock lithology are clearly less mature than the soil into which they impacted.

[50] We selected several on- and off-swirl craters for SCREP analysis using the albedo and true color images rather than the PC axis number 13 (we did not use the 2820 nm absorption depth parameter as the image was not available at the time of the SCREP analysis). This allowed us to use the spectral data to assess the spectral differences between on- and off-swirl regolith and attempt to determine if there is a compositional difference inherent in the bedrock beneath the regolith.

[51] Results from the SCREP analysis revealed several distinguishing characteristics between spectra on- and off-swirl. The most apparent characteristic is the separation into higher and lower relative albedos, which is well demonstrated in regolith spectra (Figures 13a, left, 13b, left, and 13c, left), and also evident in fresh crater spectra (Figures 13a, top, 13b, top, and 13c, top). Spectra from fresh craters that occur on-swirl have a higher overall albedo, more convex continuum shape, and deep mafic absorptions (Figures 13a, bottom, 13b, bottom, and 13c, bottom) compared with fresh craters occurring off-swirl. Off-swirl regolith spectra resemble those of typical mature surfaces [e.g., Pieters *et al.*, 1993, 2000; Hapke, 2001]. On-swirl soils rival and exceed highland reflectance, even in mare regions. In addition, on-swirl soils have strong mafic absorptions features. The 1 μm absorption is even apparent on the swirls at Gerasimovich.

[52] Off-swirl, the maturing surface darkens, although the change in albedo from immature to mature is small. Off-swirl spectra also show very little change in the continuum slope (reddening) across the M³'s spectral range. On-swirl spectra undergo a huge change in albedo, yet the mature surface remains as bright as the freshest off-swirl craters. Despite the large change in reflectance, absorption feature depths show very little change. The continuum slope increases at shorter wavelengths, but shows little change beyond ~ 1500 nm.

6. Discussion

6.1. Optical Maturity, Space Weathering and Nanophase Iron

[53] NpFe⁰ is the space weathering product that has the strongest influence on reflectance spectra, and its abundance in a soil is correlated with that soil's exposure age [e.g., Morris, 1978]. Creation of npFe⁰ is recognized as occurring in three ways: (1) sputtering, (2) impact vaporization and deposition, and (3) agglutination [e.g., Hapke *et al.*, 1975; Keller and McKay, 1993, 1997; Hapke, 2001; Noble *et al.*, 2007]. Mechanisms 1 and 2 create npFe⁰ by breaking the Fe-O bond and depositing native iron [Dukes *et al.*, 1999; Loeffler *et al.*, 2009]. These two processes typically work on very small scales (i.e., grain surfaces up to a few molecule layers deep), and create npFe⁰ particle sizes usually < 10 nm in diameter. Mechanism 3 creates larger npFe⁰ particle sizes by merging preexisting smaller ones in the high temperature melt of a micrometeoroid impact. Also during such events, smaller npFe⁰ particles are created through reduction by

implanted solar wind hydrogen, while larger sizes are created via coalescence of smaller particles. Of the two dominant agents of space weathering, micrometeorites and solar wind ions ($\sim 95\%$ of which is H⁺), the latter are the only space weathering agent that can be influenced by the enhanced magnetic field at the swirls. The magnetic fields deflects solar wind ions away from the on-swirl surfaces and focuses them onto off-swirl surfaces. Thus, on-swirl maturation is retarded because only space weathering mechanisms 1 and 3 operate on these surfaces. Off-swirl maturation may be accelerated because in addition to experiencing all three space weathering mechanisms, off-swirl surfaces could receive an enhanced H⁺ ion flux deflected from on-swirl surfaces. There are one or two spectra that were classified as off-swirl, but have spectral shapes characteristic of on-swirl SCREP spectra. This may be due to miscategorizing an analyzed crater or because the sampled off-swirl crater is fresh enough to still have the spectral signature that is preserved on-swirl by solar wind ion deflection.

[54] Solar wind ions deflected from the swirls increase the flux to the off-swirl surfaces and may become saturated with hydrogen beyond levels experienced at normal (nonswirl) areas [Zeller *et al.*, 1966; Starukhina, 2001]. In fact, hydrogen retention in the lunar soil can be enhanced by a small magnetic field, allowing it to exceed the 50–75 ppm threshold measured in Apollo soil samples [Morris, 1976]. In addition to increased amounts npFe⁰ created by an increased rate of sputtering, a meteoroid impacting the H-enriched off-swirl soils can facilitate a greater abundance of iron to be reduced in one event and in one location, leading to a more rapid generation of larger npFe⁰ particles to be formed by melting or accreting during the impact.

[55] Ions deflected from the swirls can enhance the concentration of hydrogen that is available for reactions when a micrometeorite strikes with sufficient energy to break the FeO bond via melting. The regionally abundant hydrogen is available to satisfy the oxidizing agent (oxygen), allowing a greater abundance of iron to be reduced in one event and in one location. Thus, a greater proportion of > 40 nm npFe⁰ is created, which causes the surface to darken over the entire spectral range, and quickly, without any appreciably reddening. The decreased proportion of small npFe⁰ particle sizes (compared with normal space weathering regions) may explain why there is such little spectral reddening.

6.2. Lunar Soils Properties and Space Weathering Effects on Reflectance Spectra

[56] The dust transport model and the comet/meteoroid swarm impact models imply that the role of the finest fraction of lunar soils and/or opaque minerals can explain spectra of on-swirl and off-swirl surfaces. There are three ways to change the overall spectral reflectance and absorption feature depths: (1) variation in grain size, (2) changing the abundance of opaques, and (3) changing the optical maturity.

6.2.1. Effect of Grain Size

[57] Decreasing grain size increases albedo and absorption depth simultaneously as shown in Figure 15 for pyroxene. Starting with coarse grains and moving toward finer grains (of the same material), albedo and absorption depth increase until the grain diameter is ~ 100 μm . As grain size decreases below 100 μm , albedo continues to increase, due to multiple scattering between the finer particles, but since surface

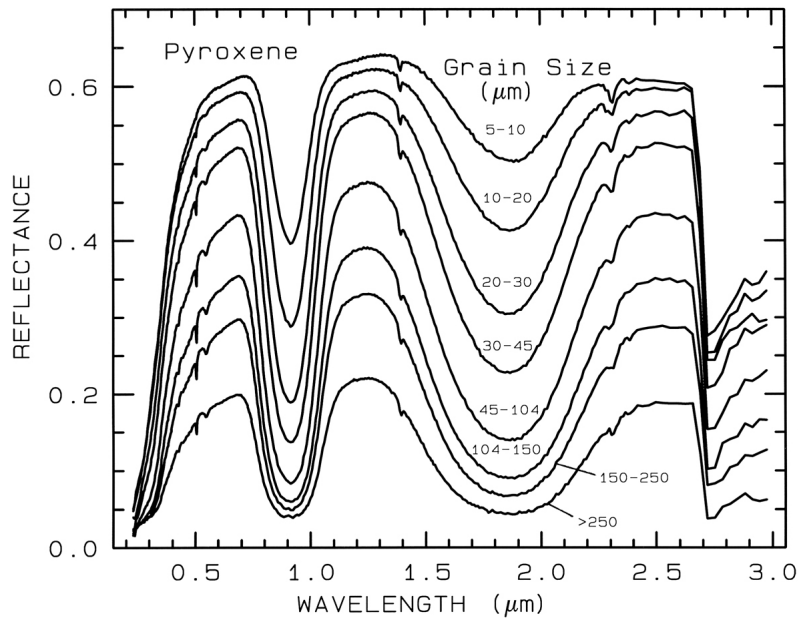


Figure 15. Reflectance spectra of pyroxene as a function of grain size. As the grain size becomes larger, more light is absorbed and the reflectance drops. From *Clark* [1999].

scattering dominates, absorption depth quickly decreases (Figure 16). Comparing spectral differences between on- and off-swirl immature craters relative to each other and their target surfaces shows that the lunar swirls cannot simply be accumulations of fine-grained material. For one thing, fresh impact craters on-swirl are still brighter than the immediately surrounding regolith (outside the crater’s own continuous ejecta blanket). Furthermore, the depth of the absorption feature decreases from fresh crater to adjacent soil, just as would be expected of a maturing material. Thus,

the observed spectral differences between on- and off-swirl materials cannot be due to different grain sizes of the same composition, as this implies that the material exposed by recent impacts is finer-grained than the surrounding regolith, which is very unlikely.

6.2.2. Effect of Opaque Mineral Phases

[58] Opaque mineral phases darken and flatten a reflectance spectrum, and can dominate the spectrum even at low concentrations. Conversely, low concentrations of opaque minerals will allow diagnostic spectral characteristics of the major phases to be observable. On the Moon, the dominant opaque phase and major titanium-bearing phase is ilmenite (Figure 17). The relationship between Ti abundance and ilmenite’s darkening effect on a reflectance spectrum was the basis for estimating TiO₂ abundance using spectra from the

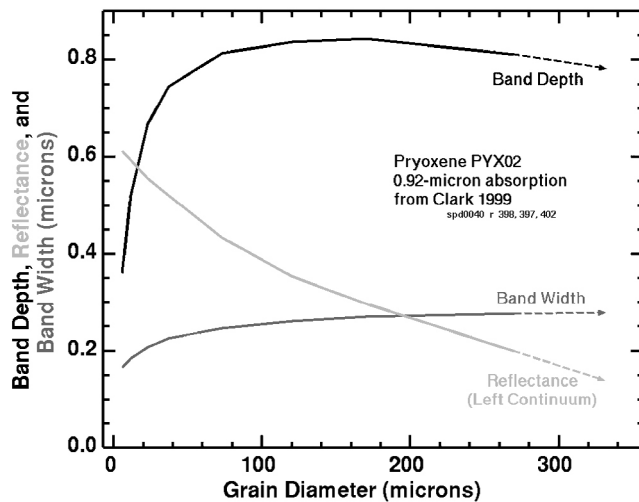


Figure 16. Trends in the absorption depth, feature width, and reflectance at 0.92 μm as a function of grain size (diameter) for pyroxene. With increasing grain size, absorption depth at first increases, reaches a peak, then decreases, while reflectance decreases and absorption feature width increases. Data from *Clark* [1999].

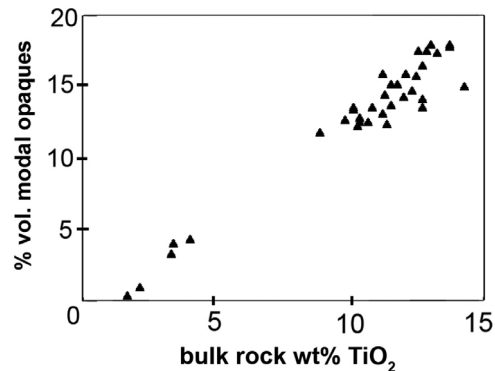


Figure 17. Modal opaque content compared with TiO₂ abundance for lunar rocks. Spread in data at high titanium concentrations due to Ti partitioning into nonopaque phases. After *Lucey et al.* [2000].

Moon [Charette et al., 1974; Blewett et al., 1997; Shkuratov et al., 1999; Lucey et al., 2000].

[59] The high albedos and strong mafic absorption features in SCREP-derived on-swirl spectra for Reiner Gamma and Mare Ingenii (Figure 13a, middle, and 13c, middle) suggest the mare basalts are low titanium. Differences in albedo are typical of impact gardening processes; mare basalt regoliths often increase slightly in overall albedo due to the continual addition of feldspathic components by large-impact ejecta from surrounding highland terrains. Mare Ingenii's brighter on-swirl regolith (compared to Reiner Gamma's) is excepted due to its closer proximity to the highlands (Figure 13c, left, and 13c, middle).

[60] More significant is the contrast between on- and off-swirl spectra. Like on-swirl soils, maturing off-swirl soils darken and mafic absorption features weaken. Although the end result of off-swirl maturation (represented by the mature off-swirl soil spectra) is a very flat, dark spectrum, even immature soil from off-swirl regions are already dark with weak absorption features; darker and weaker than on-swirl soil. Off-swirl spectra also show a limited range in albedos relative to the range exhibited in on-swirl spectra. These spectral characteristics could be explained by either (1) the selective removal of opaque minerals from fresh basalt exposures on-swirl and transport to off-swirl regions or (2) the gradual addition of opaque minerals from an exogenous source.

[61] We cannot explain a process by which ilmenite would be selectively removed from on-swirl surfaces any more than it would be to selectively move any one mineral, which argues against the first point. If one considers spectra from fresh craters to mature regolith, on-swirl trends indicate that ilmenite abundance is increasing as the surface matures. But from where would this ilmenite derive? There is no high-Ti unit in any reasonable proximity, particularly near Ingenii where this spectral effect is significant. Either there is a very exotic and unexplained phenomenon that causes selective movement of opaques between on- and off-swirl regions or something is causing the spectra to appear as such. The cause is important as it has implications for spectrally derived TiO₂ abundance estimates.

6.3. Existing Models in Light of Results From M³

[62] Summarized here are the M³ analytical results that provide the evidence upon which we assess the nature of the lunar swirls: (1) strong correlation between low OH abundance (shallow 2.82 μm absorption) and high-albedo swirls, (2) spectral maturation trends off-swirl (darkening, narrow range in albedos; reddening, very little; continuum shape, approximately constant across M³ spectral range; absorptions, subdued), and (3) spectral maturation trends on-swirl (darkening, wide range in albedos; reddening, mostly at wavelengths less than ~1500 nm; continuum shape, concave continuum changes at ~1500 nm; absorptions, relatively preserved).

6.3.1. The Dust Transport Model

[63] Clementine spectral data of the lunar swirls has been used to argue that the swirls are regions of accumulated fine dust by electrostatic transport [Garrick-Bethell et al., 2011]. One aspect of their model is that the grain size fraction (<10 μm) that would be mobilized is enriched in feld-

spathic material, and thus would explain the high albedo nature of the lunar swirls. However, the results from M³ data do not show evidence for an increased feldspathic component. As the feldspathic component of a mare soil increases, so will the surface albedo; however mafic absorption features will simultaneously become progressively weaker due to both multiple scattering from the fine grains and from the increasing proportion of plagioclase relative to basalt [Keller et al., 2000; Noble et al., 2001]. The finest fraction is considered "feldspathic" because it is abundant in Al, Ca, Si. The finest fraction of the lunar soil is composed of light-colored glass blebs (agglutinates), which *would* increase the soil albedo *if* they did not have embedded npFe⁰. However, all agglutinates studied in soils returned by the Apollo and Luna missions contain npFe⁰. With increasing maturity the concentration of feldspathic glass increases, and more importantly, the concentration npFe⁰ within the glass increases. The spectral characteristics we identify as maturity are caused by the presence of npFe⁰: the more npFe⁰ present in the soil, the more spectrally mature it appears. Given a path to interact with the light we are measuring, npFe⁰ will dominate the spectrum, and the transparent feldspathic agglutinates provide that opportunity. Therefore, the fact that the swirls look spectrally *immature* precludes a high abundance of npFe⁰; and since the processes that form the feldspathic agglutinates simultaneously create and embed npFe⁰ within them, the finest fraction could not be transported onto the swirls without npFe⁰, which would then make the swirls look mature, which they don't. While we do not find direct evidence for an increased feldspathic component, the dust transport model still has several attractive properties that suggest it may be important in controlling swirl formation.

6.3.2. The Comet/Meteoroid Swarm Impact Model

[64] The high albedo nature of the swirls was used by [Schultz and Srnka, 1980; Pinet et al., 2000; Chevrel et al., 1998, 2000] to argue that the swirls are regions where the fine-grained upper regolith was removed and/or redeposited as a result of scouring by a comet impact. Such a conclusion was based on plots comparing surface regoliths similar to, although not the same as Figure 13a (left) for Reiner Gamma. Indeed, the albedo of a material will increase as the grain size decreases. Figure 13 shows that spectra from on-swirl regions not only have a higher albedo, but the albedo is correlated with an increase in both mafic absorption features (although most noticeable at ~1 μm in Figure 13a (middle) for Reiner Gamma).

[65] Comparing on- and off-swirl mature soil and fresh impact spectra demonstrates that the swirls cannot be modeled by a mechanism that would removing the finest fraction in the soil, such as scouring by a comet (or deposit the finest fraction, as discussed above for the dust transport model). Although Pinet et al. [2000] did describe "immature mare crater-like soils" spectra as part of their analysis of Clementine UVVIS data, these spectra did not exhibit the deepest mafic absorption of the sampled spectra, which would have been a representative characteristic of the most immature spectra. Furthermore, these authors based their conclusion on the observation that the bright swirl soils at Reiner Gamma being spectrally similar to the immature mare crater-like soils. However, on-swirl immature crater spectra are distinct from off-swirl immature crater spectra in

both overall albedo and mafic absorption features (Figure 13a, middle, 13b, middle, and 13c, middle), and among all the fresh crater spectra there is very little overlap (not all sampled spectra are shown, in the interest of clarity). The sampled craters range between 0.5 and 5 km in diameter, and thus penetrate 50 to 500 meters below the surface, considerably deeper than the proposed comet scouring. If the swirl surfaces are only different from their surroundings because they are regions where the finest surface layer were removed, then there should be no such obvious difference between the fresh craters sampled on-swirl versus off-swirl, as they are supposed to be tapping the same lithology.

6.3.3. The Solar Wind Deflection Model

[66] The spectral characteristics observed with M³ data are consistent with those of *Kramer et al.* [2011] using Clementine data. They interpreted the spectra of immature sampled craters and mature soils as resulting from different rates of optical maturation. More specifically, the spectra reflect the magnetic anomaly's influence on the space weathering agents responsible for creating npFe⁰. *Hapke* [2001], *Keller and Clemett* [2001], and *Noble et al.* [2007] showed that the spectral effects of maturation are largely a function of the abundance and modal sizes of npFe⁰ particles. Smaller npFe⁰ particles (<10 nm in diameter) cause spectral reddening in the visible wavelengths, yet no appreciable effect in the NIR, which is consistent with spectra observed on-swirl. Larger particles (>40 nm) darken and flatten (attenuated absorption features) the entire VIS-NIR spectrum with little change in the continuum slope, which is consistent with off-swirl spectra. Smaller particles are created by reduction of Fe²⁺ to native iron through sputtering, vaporization, and solar wind implanted H⁺. Larger npFe⁰ particles are dominant in agglutinitic glass, and are created by merging of smaller npFe⁰ particles during the melting agglutinate-forming process by micrometeoroid impacts.

7. Conclusions

[67] M³ spectra show that relative to their surroundings, the lunar swirls have high albedos, low maturity, and low OH abundances. 2.82 μm absorption depth parameter images distinguish the swirls better than previous efforts to delineate swirls. The parameter makes swirl identification apparent, even in the highlands, and will be a useful tool for locating new swirls. The shallow 2.82 μm absorption depth on-swirl is consistent with an expected lower OH abundance on-swirl relative to off-swirl as a result of the solar wind being deflected from the surface at those locations.

[68] PCA analyses of three lunar swirls using new M³ spectral data demonstrate that the brightest areas of the swirls have the stronger mafic absorptions. For Ingenii, the mineralogical diversity of the soils may be significantly influencing the shape of the spectra, as well as the swirls. SCREP and mature regolith spectra (Figure 13) are used to demonstrate maturation trends on- and off-swirl. The spectral characteristics of on- and off-swirl surfaces reflect a spatial control on nanophase iron particle size creation and/or sorting.

[69] Observed spectral features from both analytical techniques are consistent with the solar wind deflection model [*Hood and Schubert*, 1980; *Hood et al.*, 1983; *Hood*,

1987; *Hood and Huang*, 1991]; where magnetic shielding deflects solar wind ions away from the on-swirl surfaces and focuses them onto off-swirl surfaces. The deflection of protons away from on-swirl surfaces slows the spectral effects of space weathering significantly, relative to normal lunar surfaces. Blocked solar wind protons means npFe⁰ production on-swirl is accomplished almost exclusively by micrometeorites [*Kramer et al.*, 2011]. Off-swirl maturation is accelerated because these regions experience normal space weathering mechanisms and receive an increased flux of H ions deflected from on-swirl surfaces. The observed spectral trends off-swirl suggests that the proportion of larger (>40 nm) npFe⁰ may dominate in swirl-adjacent, off-swirl locations because the hydrogen-supersaturated soil would readily reduce large amounts of Fe²⁺ upon heating from small impacts [*Kramer et al.*, 2011].

[70] The results are not consistent with the dust transport model [*Garrick-Bethell et al.*, 2011]. By inconsistent, we do not mean that particles cannot be moved to different location and accumulate to produce the high albedo features, we say that the strong absorption at 1 μm and the shallower one at 2 μm are inconsistent with an accumulation of crystalline plagioclase and/or feldspathic glassy components. However, the interpretation that the spectral characteristics of the swirls are indicators of a control on the abundance and particle sizes of npFe⁰ could be explained by the dust transport model as well as, better than, or in conjunction with the solar wind deflection model.

7.1. Potential for Mineralogical Assessment of Discrete Swirl Units

[71] M³ data provide an unprecedented opportunity to characterize the mafic mineralogy on- and off-swirl, particularly at Reiner Gamma and Mare Ingenii which occur in the maria. Differences between the pyroxene compositions on- and off-swirl are currently difficult to interpret due to apparently inconsistent behavior of the wavelengths of maximum absorption at 1 and 2 μm based on the relationship between calcium abundance in laboratory-analyzed pyroxene spectra [*Adams*, 1974; *Cloutis and Gaffey*, 1991; *Klima et al.*, 2011]. Compositional variations are observed for the pyroxenes in Mare Ingenii in particular, but these do not seem to be directly correlated with the swirls themselves. Since some of the models for swirl formation include concentration of feldspathic material or differences in space weathering, intimate mixture analysis of M³ spectra to approximate on- and off-swirl mineral abundances may help differentiate between models. The observation that typical maturation effects may be decoupled from one another on- and off-swirl and may complicate the use *Hapke's* space weathering model for radiative transfer modeling [*Hapke*, 2001] of the swirls.

7.2. Application to Studies of Optical Maturity

[72] Analysis of the lunar swirls will do much toward improving our understanding of the optical effects of space weathering. Detailed analysis of morphological features on and around lunar swirls and the relative difference between their spectral profiles could shed new light on the role of solar wind charged particles in optical maturation.

[73] **Acknowledgments.** The authors wish to thank the Indian Space Agency, ISRO, for providing the Moon Mineralogy Mapper the opportunity to ride as a guest instrument on Chandrayaan-1. The authors also wish to thank the reviewers for their efforts that went toward improving this paper.

References

- Adams, J. B. (1974), Visible and near-infrared diffuse reflectance spectra of pyroxenes as applied to remote sensing of solid objects in the solar system, *J. Geophys. Res.*, **79**, 4829–4836, doi:10.1029/JB079i032p04829.
- Bell, J. F., and B. R. Hawke (1981), The Reiner Gamma Formation—Composition and origin as derived from remote sensing observations, *Proc. Lunar Planet. Sci. Conf.*, **12**, 679–694.
- Bell, J. F., and B. R. Hawke (1987), Recent comet impacts on the Moon—The evidence from remote-sensing studies, *Publ. Astron. Soc. Pac.*, **99**, 862–867, doi:10.1086/132051.
- Besse, S., J. M. Sunshine, M. I. Staid, N. E. Petro, J. W. Boardman, R. O. Green, J. W. Head, P. J. Isaacson, J. F. Mustard, and C. M. Pieters (2011), Compositional variability of the Marius Hills volcanic complex from the Moon Mineralogy Mapper (M³), *J. Geophys. Res.*, **116**, E00G13, doi:10.1029/2010JE003725.
- Blewett, D. T., P. G. Lucey, B. R. Hawke, and B. L. Jolliff (1997), Clementine images of the lunar sample-return stations; refinement of FeO and TiO₂ mapping techniques, *J. Geophys. Res.*, **102**, 16,319–16,325, doi:10.1029/97JE01505.
- Blewett, D. T., C. G. Hughes, B. R. Hawke, and N. C. Richmond (2007), Varieties of lunar swirls, *Lunar Planet. Sci.*, **XXXVIII**, Abstract 1232.
- Blewett, D. T., B. W. Denevi, M. S. Robinson, and M. E. Purucker (2009), Do lunar-like swirls occur on Mercury?, *Lunar Planet. Sci.*, **XL**, Abstract 1352.
- Boardman, J. W., C. M. Pieters, R. O. Green, S. R. Lundeen, P. Varanasi, J. Nettles, N. Petro, P. Isaacson, S. Besse, and L. A. Taylor (2011), Measuring moonlight: An overview of the spatial properties, lunar coverage, selenolocation, and related Level 1B products of the Moon Mineralogy Mapper, *J. Geophys. Res.*, **116**, E00G14, doi:10.1029/2010JE003730.
- Campbell, B. A., L. M. Carter, D. B. Campbell, B. R. Hawke, R. R. Ghent, and J. L. Margot (2006), 20-m resolution radar studies of the Aristarchus plateau and Reiner Gamma Formation, *Lunar Planet. Sci.*, **XXXVII**, Abstract 1717.
- Charette, M. P., T. B. McCord, and C. Pieters (1974), Application of remote spectral reflectance measurements to lunar geology classification and determination of titanium content of lunar soils, *J. Geophys. Res.*, **79**, 1605–1613, doi:10.1029/JB079i011p01605.
- Chevrel, S. D., C. Rosemberg, P. C. Pinet, V. V. Shevchenko, and Y. Daydou (1998), Lunar swirl-like terrains exploration: The case of Mare Ingenii, *Lunar Planet. Sci.*, **XXIX**, Abstract 1660.
- Chevrel, S., P. Pinet, Y. Daydou, S. Maurice, W. Feldman, D. Lawrence, and P. Lucey (2000) Comparison and integration of Fe, Ti and Th abundances of the lunar surface at global scale from Clementine and gamma-ray Lunar Prospector data, in *Exploration and Utilisation of the Moon*, edited by B. H. Foing and M. Perry, *Eur. Space Agency Spec. Publ.*, **ESA SP 462**, 361–459.
- Chevrel, S., P. C. Pinet, A. Jehl, S. Besse, A. Cord, Y. Daydou, D. Baratoux, V. G. Kaydash, and Y. Shkuratov (2006), Surface physical properties of the lunar regolith at Reiner Gamma: Characterization and distribution using Hapke model inversion, *Lunar Planet. Sci.*, **XXXVII**, Abstract 1173.
- Clark, R. N. (1999), Spectroscopy of rocks and minerals, and principles of spectroscopy, in *Manual of Remote Sensing*, vol. 3, *Remote Sensing for the Earth Sciences*, pp. 3–58, John Wiley, New York.
- Clark, R. N., and T. L. Roush (1984), Reflectance spectroscopy: Quantitative analysis techniques for remote sensing applications, *J. Geophys. Res.*, **89**, 6329–6340, doi:10.1029/JB089iB07p06329.
- Clark, R. N., G. A. Swayze, K. E. Livo, R. F. Kokaly, S. J. Sutley, J. B. Dalton, R. R. McDougal, and C. A. Gent (2003), Imaging spectroscopy: Earth and planetary remote sensing with the USGS Tetracorder and expert systems, *J. Geophys. Res.*, **108**(E12), 5131, doi:10.1029/2002JE001847.
- Clark, R. N., C. M. Pieters, R. O. Green, J. W. Boardman, and N. E. Petro (2011), Thermal removal from near-infrared imaging spectroscopy data of the Moon, *J. Geophys. Res.*, **116**, E00G16, doi:10.1029/2010JE003751.
- Cloutis, E. A., and M. J. Gaffey (1991), Pyroxene spectroscopy revisited—Spectral-compositional correlations and relationship to geothermometry, *J. Geophys. Res.*, **96**, 22,809–22,826, doi:10.1029/91JE02512.
- Criswell, D. R. (1972), Lunar dust motion, *Proc. Lunar Planet. Sci. Conf.*, **3**, 2671–2680.
- Dukes, C. A., R. A. Baragiola, and L. A. McFadden (1999), Surface modification of olivine by H⁺ and He⁺ bombardment, *J. Geophys. Res.*, **104**, 1865–1872, doi:10.1029/98JE02820.
- Farmer, V. C. (1974), *The Infrared Spectra of Minerals*, *Monogr. 4*, Mineral. Soc., London.
- Fuller, M. (1974), Lunar magnetism, *Rev. Geophys.*, **12**, 23–70, doi:10.1029/RG012i001p00023.
- Fuller, M., and S. M. Cisowski (1987), Lunar paleomagnetism, *Geomagnetism*, **2**, 307–455.
- Garrick-Bethell, I., B. P. Weiss, D. L. Shuster, and J. Buz (2009), Early lunar magnetism, *Science*, **323**, 356–359, doi:10.1126/science.1166804.
- Garrick-Bethell, I., J. W. I. Head, and C. M. Pieters (2011), Spectral properties, magnetic fields, and dust transport at lunar swirls, *Icarus*, **212**, 480–492, doi:10.1016/j.icarus.2010.11.036.
- Goswami, J. N., and M. Annadurai (2009), Chandrayaan-1: India's first planetary science mission to the Moon, *Lunar Planet. Sci.*, **IX**, 2571.
- Green, R. O., C. Pieters, P. Mouroullis, M. Eastwood, J. Boardman, S. Lundeen, S. Geier, and G. Sellar (2011), The Moon Mineralogy Mapper (M³) imaging spectrometer for lunar science: Instrument, calibration, and on-orbit measurement performance, *J. Geophys. Res.*, doi:10.1029/2011JE003797, in press.
- Halekas, J. (2003), The origins of lunar crustal magnetic fields, Ph.D. thesis, Univ. of Calif., Berkeley, Calif.
- Hapke, B. (2001), Space weathering from Mercury to the asteroid belt, *J. Geophys. Res.*, **106**, 10,039–10,073, doi:10.1029/2000JE001338.
- Hapke, B., W. Cassidy, and E. Wells (1975), Effects of vapor-phase deposition processes on the optical, chemical and magnetic properties of the lunar regolith, *Moon*, **13**, 339–353, doi:10.1007/BF00567525.
- Haskin, L. A. (1998), The Imbrium impact event and the thorium distribution at the lunar highlands surface, *J. Geophys. Res.*, **103**, 1679–1689, doi:10.1029/97JE03035.
- Hawke, B. R., D. T. Blewett, E. I. Coman, M. E. Purucker, and J. J. Gillis-Davis (2009), Spectral and magnetic studies of lesser-known lunar magnetic and albedo anomalies, *Eos Trans. AGU*, **90**(52), Fall Meet. Suppl., Abstract P23C-1272.
- Hicks, M. D., B. J. Buratti, J. Nettles, M. Staid, J. Sunshine, C. M. Pieters, S. Besse, and J. Boardman (2011), A photometric function for analysis of lunar images in the visual and infrared based on Moon Mineralogy Mapper observations, *J. Geophys. Res.*, **116**, E00G15, doi:10.1029/2010JE003733.
- Hood, L. L. (1981), Sources of lunar magnetic anomalies and their bulk directions of magnetization: Further evidence from Apollo orbital data, *Proc. Lunar Planet. Sci. Conf.*, **12**, 817–830.
- Hood, L. L. (1987), A model for the formation of magnetic anomalies antipodal to lunar impact basins, *Lunar Planet. Sci.*, **XVIII**, Abstract 433.
- Hood, L. L., and N. A. Artemieva (2008), Antipodal effects of lunar basin-forming impacts: Initial 3d simulations and comparisons with observations, *Icarus*, **193**, 485–502, doi:10.1016/j.icarus.2007.08.023.
- Hood, L. L., and Z. Huang (1991), Formation of magnetic anomalies antipodal to lunar impact basins - two-dimensional model calculations, *J. Geophys. Res.*, **96**, 9837–9846, doi:10.1029/91JB00308.
- Hood, L. L., and G. Schubert (1980), Lunar magnetic anomalies and surface optical properties, *Science*, **208**, 49–51, doi:10.1126/science.208.4439.49.
- Hood, L. L., and A. Vickery (1984), Magnetic field amplification and generation in hypervelocity meteoroid impacts with application to lunar paleomagnetism, *J. Geophys. Res.*, **89**, C211–C223, doi:10.1029/JB089iS01p0C211.
- Hood, L. L., and C. R. Williams (1989), The lunar swirls—Distribution and possible origins, *Proc. Lunar Planet. Sci. Conf.*, **19**, 99–113.
- Hood, L. L., P. J. Coleman, and D. E. Wilhelms (1979), The Moon: Sources of the crustal magnetic anomalies, *Science*, **204**, 53–57, doi:10.1126/science.204.4388.53.
- Hood, L. L., R. P. Lin, and A. E. Metzger (1983), A correlative study of orbital electron reflectance and gamma ray data with surface geology on the south-central lunar far side, *Proc. Lunar Planet. Sci. Conf.*, **14**, 323–324.
- Hood, L. L., A. Zakharian, J. Halekas, D. L. Mitchell, R. P. Lin, M. H. Acuña, and A. B. Binder (2001), Initial mapping and interpretation of lunar crustal magnetic anomalies using Lunar Prospector magnetometer data, *J. Geophys. Res.*, **106**, 27,825–27,839, doi:10.1029/2000JE001366.
- Hughes, C. G., D. T. Blewett, B. R. Hawke, and N. C. Richmond (2006), Optical maturity and magnetic studies of lunar swirls, *Lunar Planet. Sci.*, **XXXVII**, Abstract 1230.
- Kaydash, V., M. Kreslavsky, Y. Shkuratov, S. Gerasimenko, P. Pinet, J.-L. Josset, S. Beauvivre, and B. Foing, and the AMIE SMART-1 Team (2009), Photometric anomalies of the lunar surface studied with SMART-1 AMIE data, *Icarus*, **202**, 393–413, doi:10.1016/j.icarus.2009.03.018.
- Keller, L. P., and S. J. Clemett (2001), Formation of nanophase iron in the lunar regolith, *Lunar Planet. Sci.*, **XXXII**, Abstract 2097.
- Keller, L. P., and D. M. McKay (1993), Discovery of vapor deposits in the lunar regolith, *Science*, **261**, 1305–1307, doi:10.1126/science.261.5126.1305.

- Keller, L. P., and D. M. McKay (1997), The nature and origin of rims on lunar soil grains, *Geochim. Cosmochim. Acta*, *61*, 2331–2341, doi:10.1016/S0016-7037(97)00085-9.
- Keller, L. P., S. J. Wentworth, D. S. McKay, L. A. Taylor, C. Pieters, and R. V. Morris (2000), Space weathering in the fine size fractions of lunar soils: Mare/highland differences, *Lunar Planet. Sci.*, *XXXI*, Abstract 1655.
- Keller, W. D., and E. E. Pickett (1950), The absorption of infrared radiation by clay minerals, *Am. J. Sci.*, *248*(4), 264, doi:10.2475/ajs.248.4.264.
- Kletetschka, G., F. Freund, P. J. Wasilewski, V. Mikula, and T. Kohout (2009), Antipodal magnetic anomalies on the Moon, contributions from impact induced currents due to positive holes and flexoelectric phenomena and dynamo, *Lunar Planet. Sci.*, *XL*, Abstract 1854.
- Klima, R. L., M. D. Dyar, and C. M. Pieters (2011), Near-infrared spectra of clinopyroxenes: Effects of calcium content and crystal structure, *Meteorit. Planet. Sci.*, *46*, 379–395, doi:10.1111/j.1945-5100.2010.01158.x.
- Kramer, G. Y. (2010), Characterizing bedrock lithologies using small crater rim and ejecta probing (SCREP), *Adv. Space Res.*, *45*(10), 1257–1267, doi:10.1016/j.asr.2009.12.006.
- Kramer, G., J. Combe, and T. McCord (2007), Characterizing lunar crustal geology, *Eos Trans. AGU*, *88*(52), Fall Meet. Suppl., Abstract P41A-0201.
- Kramer, G. Y., B. L. Jolliff, and C. R. Neal (2008), Distinguishing high-alumina mare basalts using Clementine UVVIS and Lunar Prospector GRS data: Mare Moscoviense and Mare Nectaris, *J. Geophys. Res.*, *113*, E01002, doi:10.1029/2006JE002860.
- Kramer, G. Y., J.-P. Combe, E. M. Harnett, B. R. Hawke, S. K. Noble, D. T. Blewett, T. B. McCord, and T. A. Giguere (2011), Characterization of lunar swirls at Mare Ingenii: A model for space weathering at magnetic anomalies, *J. Geophys. Res.*, *116*, E04008, doi:10.1029/2010JE003669.
- Kreslavsky, M. A., and Y. G. Shkuratov (2003), Photometric anomalies of the lunar surface: Results from Clementine data, *J. Geophys. Res.*, *108*(E3), 5015, doi:10.1029/2002JE001937.
- Lawrence, K. P., and C. L. Johnson (2009), Magnetic characterization of lunar samples: Back to basics, *Lunar Planet. Sci. Conf.*, *XL*, Abstract 1433.
- Loeffler, M. J., C. A. Dukes, and R. A. Baragiola (2009), Irradiation of olivine by 4 keV He⁺: Simulation of space weathering by the solar wind, *J. Geophys. Res.*, *114*, E03003, doi:10.1029/2008JE003249.
- Longmire, C. (1963), *Elementary Plasma Physics*, Interscience, New York.
- Lucey, P. G., D. T. Blewett, and B. R. Hawke (2000), Lunar iron and titanium abundance algorithms based on final processing of Clementine ultraviolet-visible images, *J. Geophys. Res.*, *105*, 20,297–20,305, doi:10.1029/1999JE001117.
- McCord, T. B., and J. B. Adams (1973), Progress in remote optical analysis of lunar surface composition, *Moon*, *7*, 453–474, doi:10.1007/BF00564646.
- Melosh, H. J. (1989), *Impact Cratering: A Geologic Process*, Oxford Univ. Press, New York.
- Morris, R. V. (1976), Surface exposure indices of lunar soils—A comparative FMR study, *Proc. Lunar Planet. Sci. Conf.*, *7*, 315–335.
- Morris, R. V. (1978), The surface exposure/maturity of lunar soils—Some concepts and I_s/FeO compilation, *Proc. Lunar Planet. Sci. Conf.*, *9*, 2287–2297.
- Nettles, J. W., et al. (2011), Optical maturity variation in lunar spectra as measured by Moon Mineralogy Mapper data, *J. Geophys. Res.*, *116*, E00G17, doi:10.1029/2010JE003748.
- Noble, S. K., C. M. Pieters, L. A. Taylor, R. V. Morris, C. C. Allen, D. S. McKay, and L. P. Keller (2001), The optical properties of the finest fraction of lunar soil: Implications for space weathering, *Meteorit. Planet. Sci.*, *36*, 31–42, doi:10.1111/j.1945-5100.2001.tb01808.x.
- Noble, S. K., C. M. Pieters, and L. P. Keller (2007), An experimental approach to understanding the optical effects of space weathering, *Icarus*, *192*, 629–642, doi:10.1016/j.icarus.2007.07.021.
- Pieters, C., E. Fischer, O. Rode, and A. Basu (1993), Optical effects of space weathering: The role of the finest fraction, *J. Geophys. Res.*, *98*, 20,817–20,824, doi:10.1029/93JE02467.
- Pieters, C. M., L. A. Taylor, S. K. Noble, L. P. Keller, B. Hapke, R. V. Morris, C. C. Allen, D. S. McKay, and S. Wentworth (2000), Space weathering on airless bodies: Resolving a mystery with lunar samples, *Meteorit. Planet. Sci.*, *35*, 1101–1107, doi:10.1111/j.1945-5100.2000.tb01496.x.
- Pieters, C. M., et al. (2009), Character and spatial distribution of possible OH/H₂O on the surface of the Moon seen by M³ on Chandrayaan-1, *Science*, *326*, 568–572, doi:10.1126/science.1178658.
- Pinet, P. C., V. V. Shevchenko, S. D. Chevrel, F. Bellagh, and C. Rosemberg (1995), Reiner Gamma Formation: Optical, spectroscopic and polarimetric properties from clementine and earthbased data, *Lunar Planet. Sci. Conf.*, *XXVI*, Abstract 1125.
- Pinet, P. C., V. V. Shevchenko, S. D. Chevrel, Y. Daydou, and C. Rosemberg (2000), Local and regional lunar regolith characteristics at Reiner Gamma Formation: Optical and spectroscopic properties from Clementine and Earth-based data, *J. Geophys. Res.*, *105*, 9457–9475, doi:10.1029/1999JE001086.
- Richmond, N. C., L. L. Hood, D. L. Mitchell, R. P. Lin, M. H. Acuña, and A. B. Binder (2005), Correlations between magnetic anomalies and surface geology antipodal to lunar impact basins, *J. Geophys. Res.*, *110*, E05011, doi:10.1029/2005JE002405.
- Schultz, P. H., and D. E. Gault (1975), Seismic effects from major basin formations on the Moon and Mercury, *Moon*, *12*, 159–177, doi:10.1007/BF00577875.
- Schultz, P. H., and L. J. Srnka (1980), Cometary collisions on the Moon and Mercury, *Nature*, *284*, 22–26, doi:10.1038/284022a0.
- Shevchenko, V. (1994), The age and frequency of recent cometary impacts on the Moon from the analysis of swirls, *Astron. Rep.*, *36*(6), 831–838.
- Shevchenko, V. V., P. C. Plinet, and S. Chevrel (1994), Remote sensing studies of immature soils on the Moon (Reiner-Gamma Formation), *Space Sci. Rev.*, *27*(4), 16–30.
- Shkuratov, Y. G., V. G. Kaydash, and N. V. Opanasenko (1999), Iron and titanium abundances and maturity degree distribution on the lunar nearside, *Icarus*, *137*, 222–234, doi:10.1006/icar.1999.6046.
- Staid, M. I., and C. M. Pieters (2000), Integrated spectral analysis of mare soils and craters: Application to eastern nearside basalts, *Icarus*, *145*, 122–139, doi:10.1006/icar.1999.6319.
- Starukhina, L. V. (2001), Water detection on atmosphereless celestial bodies: Alternative explanations of the observations, *J. Geophys. Res.*, *106*, 14,701–14,710, doi:10.1029/2000JE001307.
- Starukhina, L. V. (2007), Meteorite swarm encounters as a source of magnetic anomalies on the lunar and mercurian surfaces, *Lunar Planet. Sci.*, *XXXVIII*, Abstract 1299.
- Starukhina, L. V., and Y. G. Shkuratov (2004), Swirls on the Moon and Mercury: Meteoroid swarm encounters as a formation mechanism, *Icarus*, *167*, 136–147, doi:10.1016/j.icarus.2003.08.022.
- Stuart-Alexander, D. E. (1978), Geologic map of the central far side of the Moon, *U.S. Geol. Surv. Misc. Invest. Ser.*, *1-1047*.
- Sunshine, J. M., T. L. Farnham, L. M. Feaga, O. Groussin, F. Merlin, R. E. Milliken, and M. F. A'Hearn (2009), Temporal and spatial variability of lunar hydration as observed by the Deep Impact spacecraft, *Science*, *326*, 565–568, doi:10.1126/science.1179788.
- Wieser, M., S. Barabash, Y. Futaana, M. Holmström, A. Bhardwaj, R. Sridharan, M. B. Dhanya, A. Schaufelberger, P. Wurz, and K. Asamura (2010), First observation of a mini-magnetosphere above a lunar magnetic anomaly using energetic neutral atoms, *Geophys. Res. Lett.*, *37*, L05103, doi:10.1029/2009GL041721.
- Wilhelms, D. (1987), The geologic history of the Moon, *U.S. Geol. Surv. Prof. Pap.*, *1348*.
- Yingst, R. A., and J. W. Head (1997), Volumes of lunar lava ponds in South Pole-Aitken and Orientale basins: Implications for eruption conditions, transport mechanisms, and magma source regions, *J. Geophys. Res.*, *102*, 10,909–10,931, doi:10.1029/97JE00717.
- Zeller, E. J., L. B. Ronca, and P. W. Levy (1966), Proton-Induced Hydroxyl Formation on the Lunar Surface, *J. Geophys. Res.*, *71*, 4855–4860, doi:10.1029/JZ071i020p04855.
- Zook, H. A., and J. E. McCoy (1991), Large scale lunar horizon glow and a high altitude lunar dust exosphere, *Geophys. Res. Lett.*, *18*, 2117–2120, doi:10.1029/91GL02235.

S. Besse, Department of Astronomy, University of Maryland, College Park, MD 20742-2421, USA.

J. W. Boardman, Analytical Imaging and Geophysics LLC, 4450 Arapahoe Ave., Ste. 100, Boulder, CO 80305, USA.

R. N. Clark, U.S. Geological Survey, MS964, Box 25046, Federal Center, Denver, CO 80225, USA.

J.-P. Combe, G. Kramer, and T. B. McCord, Bear Fight Institute, 22 Fiddler's Rd., Box 667, Winthrop, WA 98862, USA. (kramer@lpi.usra.edu)

D. Dhingra, J. W. Head, J. W. Nettles, and C. M. Pieters, Department of Geological Sciences, Brown University, Box 1846, Providence, RI 02912, USA.

I. Garrick-Bethell, Department of Earth and Planetary Sciences, University of California, Santa Cruz, CA, USA.

R. L. Klima, Johns Hopkins University Applied Physics Laboratory, 11100 Johns Hopkins Rd., Laurel, MD 20732-0000, USA.

L. A. Taylor, Planetary Geosciences Institute, Department of Earth and Planetary Sciences, University of Tennessee, 1412 Circle Dr., Knoxville, TN 37996-1410, USA.